



JGR Oceans

RESEARCH ARTICLE

10.1029/2023JC019924

Key Points:

- A new model framework is developed to parameterize subglacial discharge plumes in the Regional Ocean Modeling System
- The model framework incorporates an outflow parameterization and three coupling options
- The model is able to reproduce the strong jet-like outflowing plume observed in a Greenlandic fjord

Supporting Information:

Supporting Information may be found in the online version of this article.

Correspondence to:

C. Wang, wangchuning@sjtu.edu.cn

Citation:

Wang, C., Chant, R. J., & Jackson, R. H. (2023). Parameterizing subglacial discharge in modeling buoyancy driven flow in tidewater glacier fjords. *Journal of Geophysical Research: Oceans*, 128, e2023JC019924. https://doi.org/10.1029/2023JC019924

Received 12 APR 2023 Accepted 10 AUG 2023

Parameterizing Subglacial Discharge in Modeling Buoyancy Driven Flow in Tidewater Glacier Fjords

Chuning Wang^{1,2}, Robert J. Chant², and Rebecca H. Jackson²

¹School of Oceanography, Shanghai Jiao Tong University, Shanghai, China, ²Department of Marine and Coastal Sciences, Rutgers, The State University of New Jersey, New Brunswick, NJ, USA

Abstract In tidewater glacier fjords, subglacial discharge drives a significant mixing mechanism near glacier fronts and drives a strong exchange flow. Numerous studies (Cowton et al., 2015, https://doi. org/10.1002/2014jc010324; Slater et al., 2017, https://doi.org/10.1002/2016gl072374) have utilized a parameterization for buoyant plume theory to force fjord scales systems, but neglect to parameterize the outflowing of the plume away from the glacial wall after it has reached its neutral density. In this study, a new model framework, ROMS-ICEPLUME, is developed to parameterize the rising and initial outflowing stage of subglacial discharge plumes in the Regional Ocean Modeling System. The coupled model applies a novel parameterization algorithm to prescribe the velocity and vertical extent of the outflowing plume, which reduces numerical instability and improves model performance. The model framework is tested with a quasi-realistic forcing using observations of a subglacial discharge plume hydrographic surveys collected from a Greenland fjord. We find that the new model framework is able to reproduce the strong outflowing plume and the compensating inflow at depth, with a spatial structure that correlates well with in-situ observations. On the other hand, the model framework without the new parameterization algorithm fails to capture the outflowing plume structure. Thus, our new framework for parameterizing subglacial discharge plumes is an improvement from previous coupled model frameworks, and is a promising tool toward advancing our understanding of circulation in tidewater glacier fjords.

Plain Language Summary In Greenland, glacier meltwater enters tidewater glacier fjords from the base of marine-terminating glaciers, drives strong upwelling plumes, and overturns large amounts of deep fjord water to the fjord surface. We developed a new model framework to represent the subglacial upwelling plume, in order to simulate the ocean circulation near a marine-terminating glacier front. The model is validated with field observations collected in a Greenlandic fjord, showing good agreement in near glacier velocity fields. This model framework is a promising tool to advance our knowledge of oceanographic processes in tidewater glacier fjords.

1. Introduction

The melting of Greenland's tidewater glaciers is one of the major contributors of the Greenland Ice Sheet mass loss (Mouginot et al., 2019; Straneo & Heimbach, 2013). At the glacier/ocean boundary, freshwater from subglacial discharge drives strong convection near the glacier front, which develops into turbulent buoyant upwelling plumes that enhance glacier melting during the summer (Straneo & Cenedese, 2015). The development of an upwelling plume is often represented by coupling buoyant plume theory (BPT) with a melt parameterization (Cowton et al., 2015; Jenkins, 2011; Morton et al., 1956) to determine the physical properties of the buoyant plume.

When injected from the base of marine-terminating glaciers, subglacial discharge is positively buoyant and drives upwelling along the glacier front that entrains ambient water. Entrainment of dense water reduces the plume's buoyancy, causing its ascent to decelerate until its vertical momentum becomes zero or it reaches the sea-surface, which marks the termination of a vertical upwelling plume. If the plume overshoots its level of neutral buoyancy before reaching the surface, it will subduct and oscillate around its level of neutral buoyancy as it starts flowing horizontally into the fjord as an "outflowing plume" (Figure 1). During these three stages, plume water is modified by mixing and eventually stabilizes at a neutral buoyant depth and propagates downstream as gravity currents (Baines, 2008). Thus, the development of a subglacial discharge plume can be divided into three stages (a) the upwelling stage, in which buoyancy is positive and the plume accelerates vertically; (b) the overshooting stage,

© 2023. American Geophysical Union. All Rights Reserved.

WANG ET AL. 1 of 21

21699291, 2023, 8, Downloaded from https://agupubs.onlinelibrary.wiley.com/doi/10.1029/2023JC019924 by Rutgers University Libraries, Wiley Online Library on [27/08/2025]. See the Terms

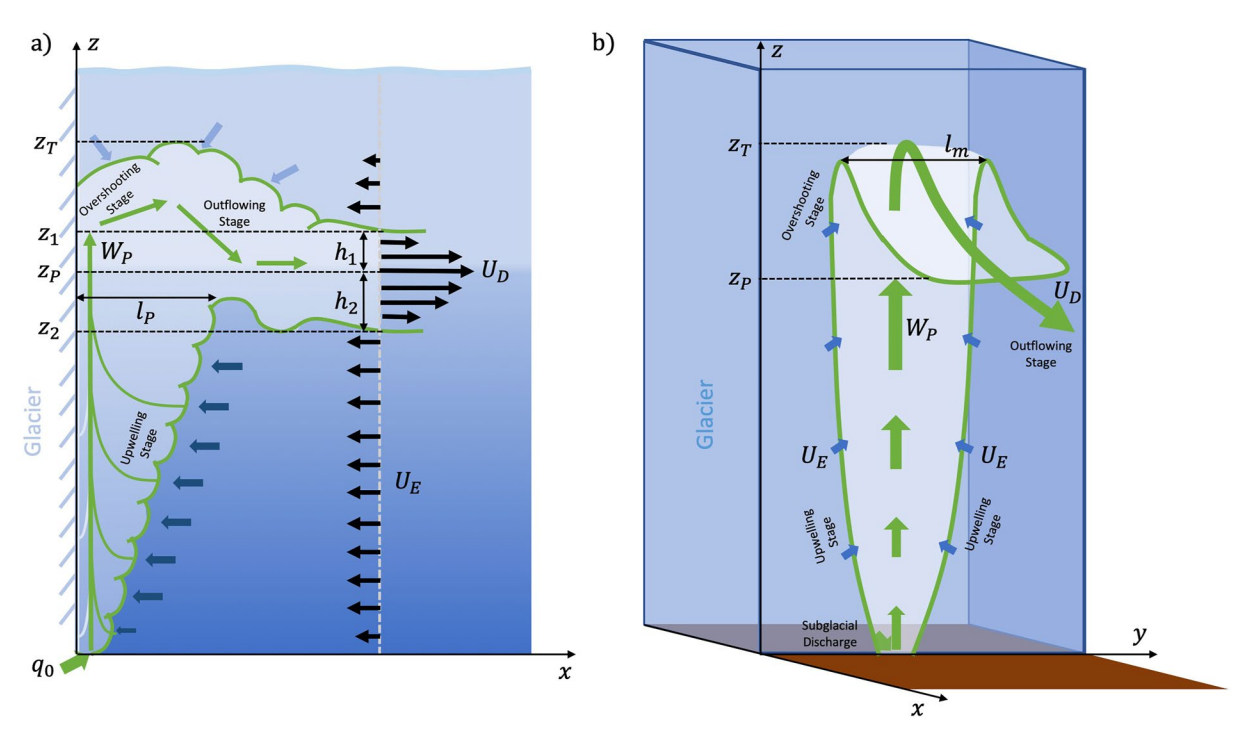


Figure 1. Schematic diagram of the development of a subglacial buoyant plume. (a) Side view of buoyant plume. The tidewater glacier is located at the left end; q_0 is the subglacial discharge rate at the base of glacier. The buoyant plume rises against the wall and terminates at depth z_T , which marks the end of the overshooting stage. The buoyant plume then travels as a gravity current, subducts to the neutral buoyant depth z_P and outflows into the fjord. (b) 3-D schematic of the development of buoyant plume.

in which buoyancy is negative and plume decelerates vertically; and (c) the outflowing stage, in which the plume gains horizontal momentum and flows downstream away from the glacier.

The initial outflowing movement of a buoyant plume near the glacier front is difficult to observe in situ or remotely and has been largely studied using numerical models or laboratory experiments (e.g., Baines, 2002; Ching et al., 1993; McConnochie et al., 2020; Xu et al., 2012, 2013). Conventional hydrographic surveys are difficult to obtain near glaciers due to the harsh environment. In addition, the buoyant plume sometimes emerges subsurface, making it difficult to detect using remote sensing techniques such as satellites or radars that are used to characterize conventional river plumes (Kilcher & Nash, 2010). In early works, the outflowing plume and its structure are often identified using its temperature and salinity characteristics based on data of near-terminus hydrographic surveys (Mortensen et al., 2011; Stevens et al., 2016); due to a lack of direct measurements of velocity, the strength and structure of the outflow and thus the exchange flow it drives are not clear and can only be inferred from its hydrographic field. Recently, a series of observational programs have quantified more aspects of discharge plumes in both Greenlandic and Alaskan fjords (e.g., Jackson et al., 2017; Mankoff et al., 2016; Motyka et al., 2013). These programs collected in-situ observations of velocity and water properties in vicinity of the glacier front and captured the flow structure during the initial outflowing stage of the plume. Even so, direct measurements of the velocity fields of subglacial discharge plumes are overall sparse; due to the sparsity, these measurements do not capture the transition from the plumes' upwelling/overshooting stage to their outflowing stage, and thus do not provide a framework to predict the outflowing stage dynamics from their upwelling and overshooting stage.

In addition to field observations, several different approaches have been taken to directly resolve or parameterize the buoyant plume in numerical models. Slater et al. (2018) used near glacier survey data from Sarqardleq fjord to drive circulation close to a glacier front in a numerical simulation. In the simulation, observed near-glacier velocity profiles are used as boundary condition to force an exchange flow driven by the upwelling plume, and the modeled circulation agrees well with simultaneous observations of velocity field. While this method produces an accurate reconstruction of the near field velocity, it requires high resolution data near the glacier front, which is rare for the reasons stated above. A variety of small-scale models have directly simulated the

WANG ET AL. 2 of 21

development of a subglacial discharge plume, including its upwelling phase, using 3-D non-hydrostatic models (Ezhova et al., 2018; Kimura et al., 2014; Xu et al., 2012) or 2-D models (Sciascia et al., 2013; Xu et al., 2012). However, this method requires a non-hydrostatic setup as well as very high horizontal and vertical resolution (1 \sim 10 m), which is computationally expensive, prohibiting fjord scale (\sim 100 km) simulations.

A third approach, which we follow and build upon in this paper, is to drive the ocean model with a parameterization of an upwelling buoyant plume, which has been used in recent modeling works (Carroll et al., 2017; Cowton et al., 2015; Oliver et al., 2020). It avoids the need to fully resolve the non-hydrostatic processes, requires only intermediate temporal and spatial resolution, and allows for fjord-scale simulations. In this paper we advance this approach by adding a parameterization of the adjustment of the plume after it detaches from the glacier and adjusts into the ambient flow and stratification that are explicitly modeled by ROMS. We refer to this region as the "detrainment" region and use a number of theoretical and laboratory studies to develop the parameterization. Furthermore, our parameterization provides an estimate of vertical structure of the detrained flow and thus uses physical reasoning to determine the vertical distribution of the outflow in the model grid. Previous studies either force the outflow in a single grid that prescribe unrealistic high vertical convergence/divergence that set prohibitive restrictions set by the Courant-Friedrichs-Lewy (CFL) condition (Cowton et al., 2015) or arbitrarily spreading the outflowing plume across a number of grids to prevent such computational restrictions (Zhao et al., 2023).

In this study, a new model framework, ROMS-ICEPLUME, is developed to parameterize all three stages—upwelling, overshooting, and outflowing—in the Regional Ocean Modeling System (ROMS, Haidvogel et al., 2008). The model framework includes (a) the general circulation model ROMS, (b) parameterization of the upwelling and overshooting stage with BPT, as is used in MITgcm (Cowton et al., 2015) (c) a novel implementation of an outflow parameterization, and (d) three coupler options to integrate the upwelling parameterization (BPT), the outflow parameterization and ROMS. In Section 2, the outflow parameterization, coupling methods, and three testing experiments are described in detail; in Section 3, results of the experiments are reported and compared with in situ observations; in Section 4, the combinations of outflow parameterization and coupling methods are discussed, and some uncertainties of the model framework are presented.

2. Methods

We developed a new module for ROMS named ICEPLUME, which uses BPT to parameterize the upwelling and overshooting stages and includes an additional parameterization for the numerically unresolved mixing and adjustment of the plume after it detaches from the wall and fully adjusts into the larger scale flow that is resolved by the numerical model. The module name ICEPLUME is inherited from the MITgcm package "iceplume" developed by Cowton et al. (2015), which for the first time implemented the BPT parameterization in a GCM to parameterize the upwelling stage of a subglacial buoyant plume. BPT computes the plume volume flux, tracer concentrations, velocity and thickness, as a function of depth in the upwelling phase, but it does not parameterize the characteristics of the horizontal outflow, such as thickness and velocity. The parameterization developed here uses the information provided by BPT and a new "detrainment" parameterization that together calculates the thickness, structure and buoyancy of the outflow rates at various depth and reports them back to ROMS to drive the fjord circulation.

Numerous studies have used BPT to force fjord scale simulations (Bao & Moffat, 2023; Cowton et al., 2015; Hager et al., 2022; Oliver et al., 2020; Slater et al., 2017; Zhao et al., 2022, 2023). For example, Cowton et al. (2015) prescribed the outflowing volume flux as vertical mass transport into a single grid cell and was implemented by prescribing vertical convergence/divergence at the top/bottom boundary of each grid cell, which is equivalently vertical velocity for a fixed grid cell surface. The size of the grid cell is arbitrary determined in the z-coordinate GCM and thus prescribed flow speed increases with vertical resolution and the outflow velocity is determined by grid resolution rather than physical reasoning. This method is convenient to implement, but the outflowing plume velocity increases with increased grid resolution, which can generate instabilities in tracer fields. To prevent prohibitive CFL restrictions, Zhao et al. (2023) arbitrarily distributed the outflow over 5 horizontal and 3 vertical grids. Due to higher shear associated with the arbitrarily prescribed outflow velocities, mixing by turbulent closure schemes, circulation and other critical properties will potentially be a function of model resolution if the initial outflow velocity is sensitive to grid size. Therefore, in high-resolution simulations the outflowing plume should be distributed in several grid cells to prescribe realistic outflow velocities and avoid numerical instabilities as well as excessive mixing

WANG ET AL. 3 of 21

due to immoderately prescribed vertical shear. Thus, we have developed an outflowing parameterization that prescribes the structure of the outflow that is based on existing theory and published laboratory experiments of this phenomenology.

We next describe the outflow parameterization and three different model implementations to represent the initial outflowing of the plume. In Section 2.1, we describe the parameterization algorithm that estimates the velocity and vertical structure of the outflowing plume; in Section 2.2, we present the strategies to couple the plume-driven volume fluxes with the GCM; in Section 2.3, we discuss the ROMS implementation of outflow parameterization and coupler; in Section 2.4, we present three numerical experiments used to test the ROMS implementation.

2.1. Outflow Parameterization

To simplify the problem, the ambient stratification in the fjord is represented with a two-layer setup, where $\rho_1 < \rho_2$ are average densities of the upper and lower layer, respectively; $g' = g(\rho_2 - \rho_1)/\rho_{\rm ref}$ is defined as the reduced gravity between two layers; $\rho_{\rm ref}$ is a reference density and g is the gravitational acceleration. As the subglacial discharge plume rises along the glacier, the plume properties are predicted by the BPT. The plume density is ρ_p when the plume's vertical velocity becomes zero. If the value of ρ_p falls between the densities of the two layers $(\rho_1 < \rho_p < \rho_2)$, the outflowing plume forms near the density interface; otherwise, the plume outflows at the surface and travels downstream as surface gravity current. Assuming that the plume detrains as one uniform water mass, the nose speed U_D of the outflowing current is estimated with an empirical parameterization developed by Ching et al. (1993) and Noh et al. (1992). For outflow in a two-layer fluid, the nose velocity is dependent on a modified Richardson number

$$Ri = \frac{g'l_P}{W_P^2} \tag{1}$$

where l_P is a length scale of the buoyant plume (roughly the along fjord width of the upwelling plume, Figure 1), and W_P is the scale of vertical velocity of the plume during the rising stage. Both l_P and W_P are predicted by the BPT. The outflow velocity is then calculated using a piecewise empirical function from Ching et al. (1993).

$$U_D = \begin{cases} 0.7Ri^{0.17}W_P, & Ri \le 6\\ 0.95W_P, & Ri > 6 \end{cases}$$
 (2)

When stratification is weak or the plume is energetic (Ri < 6), the upwelling plume overshoots far into the top layer, and the transition from an upwelling plume to a horizontal outflow is very slow. Therefore, the outflow adjusts as a function of Richardson Number, coinciding with the behavior of a gravity current. When stratification is strong (Ri > 6), the overshooting phase is short, and the density interface acts like a solid boundary (McConnochie et al., 2020) which redirects the momentum from vertical to horizontal direction (with a 5% loss), thus the dependence on Richardson Number is weak and nose velocity is scaled with W_p . When stratification is very weak, or the plume is strong, the plume density can be smaller than the surface layer the outflow emerges at the surface. In this case the air-sea interface can be seen as a very strong density interface, and the expression for high Richardson Number (Ri > 6) is adopted to determine the nose velocity of a surface outflow.

The next step is to determine the velocity structure of the outflow which we based on the velocity profiles reported by Baines (2002) and Ching et al. (1993). We use an asymmetric Gaussian function to approximate the velocity profile; the Gaussian shape is able to generate a smooth transition from the core of outflow to the ambient water, and reduces the artificial mixing caused by unrealistically high shear if the flow is injected in a single layer.

The assumed expression of the Gaussian velocity profile is

$$u_D(z) = \begin{cases} U_D \exp\left[-0.5\left(\frac{1}{\sigma} \frac{z - Z_P}{h_2}\right)^2\right], & Z_P - h_2 < z < Z_P \\ U_D \exp\left[-0.5\left(\frac{1}{\sigma} \frac{z - Z_P}{h_1}\right)^2\right], & Z_P < z < Z_P + h_1 \end{cases}$$
(3)

WANG ET AL. 4 of 21

This expression is asymmetric around the outflow core depth Z_p ; on either side it is normalized by length scales h_1 , h_2 , which we define later. We have chosen $\sigma = 0.5$ so that over 95% of the outflow is contained between $Z_p + h_1$ and $Z_p - h_2$ while the vertical shear is relatively linear throughout most of the outflowing plume.

The corresponding outflow volume flux (per unit depth) is $q_D(z) = l_m u_D(z)$, where l_m is the "width" of the plume (Figure 1) predicted by BPT. The total outflow volume flux is then $Q_D = \int_{Z_P - h_2}^{Z_P + h_1} q_D(z) dz$, which is equivalent to the upwelling plume volume flux predicted by BPT; since the profile is Gaussian on either side, its integration can be easily computed. Therefore, the total thickness of the outflow is

$$h \equiv h_1 + h_2 = \frac{Q_D}{l_m U_D \int_{-1}^{1} \exp\left[-0.5(\tilde{z}/\sigma)^2\right] d\tilde{z}}$$
(4)

When a gravity current intrudes into a two-layer stratified fluid, it forms a downstream traveling "nose" along the interface. The shape and thickness of the nose (and thus the interface) is determined jointly by densities of the two layers and the velocity of the outflowing plume, and in most cases it is asymmetric around the layer boundary (Ungarish, 2010). Therefore, the plume will be vertically asymmetric around Z_P when $I_1 \neq I_2$ (Figure 1).

To calculate h_1 and h_2 we follow Ungarish (2010) and match the pressure at the base of outflow with the pressure of the ambient water of the same depth. When the buoyant plume detrains from the glacier front, it pushes ambient water downstream and changes the local pressure. The pressure at the bottom of the outflow (Z_2 in Figure 1) is estimated by integrating from surface

$$P_2 = P_0 + g[\rho_1(Z_P - h_1) + \rho_P(h_1 + h_2)]$$
(5)

where P_0 is the atmospheric pressure. By ignoring any deflections at the free-surface, the ambient water pressure at the same depth is

$$P_2' = P_0 + g(\rho_1 Z_P + \rho_2 h_2) \tag{6}$$

The "steady" condition for gravity current intrusion requires $P_2 = P'_2$. When $P_2 < P'_2$, the dense ambient water (ρ_2) is forced to move upstream, lifting the buoyant plume to a shallower depth; when $P_2 > P'_2$, the outflow water mass sinks and pushes the ambient water downstream. Rearranging Equations 4–6 gives

$$h_{1} = \frac{\rho_{P} - \rho_{1}}{\rho_{2} - \rho_{1}} h,$$

$$h_{2} = \frac{\rho_{2} - \rho_{P}}{\rho_{2} - \rho_{1}} h$$
(7)

This formulation only applies to a two-layer configuration. In a continuously stratified environment, ρ_1 and ρ_2 are the mean densities above and below Z_P , but when integrating pressure from surface to Z_2 , the "steady" condition criterion $P_2 = P_2'$ may not be met. Thus, in our numerical application h_1 and h_2 are determined by an iterative search of grids in the vicinity of Z_P until the total thickness is greater than h; more details of the algorithm are provided in Supporting Information S1.

In summary, the total volume flux q_D and tracer properties (salinity, temperature and passive tracers) of the outflowing plume are determined by BPT, while velocity, shear and thickness of the initial outflow are determined by the outflow parameterization. No additional mixing or horizontal spreading is applied during the transition from an upwelling plume to an outflowing plume, thus the temperature, salinity and volume flux of the plume are not changed in the transition stage. Combined, these two steps predict the entrainment and outflowing rates driven by subglacial discharge, which are used to calculate volume and tracer fluxes at the boundary of the ocean model.

2.2. Coupling BPT With GCM

The subglacial channels are relatively narrow compared to the width of glacier front. As a result, unlike a river channel, the outflowing plume near the glacier front is not limited by lateral boundaries and will spread laterally. Here we develop three different methods to prescribe the outflowing plume into the GCM. The first, we call \mathbf{H}_{Mass} , prescribes a horizontal mass flux and is inspired by field observations of a jet-like outflow in the vicinity

WANG ET AL. 5 of 21

of the glacier (Jackson et al., 2017). A second follows the implementation in MITgcm that prescribes a convergent vertical mass flux, we call V_{Mass} that then drives a horizontal flow at the boundary. Both of these prescribe strong velocities which may require shortening the model's time step to avoid violating the CFL condition. To alleviate this, we offer a third scheme we call Mix, which prescribes the outflow without initial horizontal momentum in the along channel direction, and the outflow behaves more isotropic and balloons out in all direction. On the other hand, H_{Mass} prescribes the outflow with momentum in the along channel direction, thus producing a jet-like flow in the near field. The outflow produced by H_{Mass} is significantly different from V_{Mass} and Mix, and is more consistent with the observations that we show in this paper.

Once the entrainment/outflowing rates are calculated, the fluxes are added to the ROMS grid as point sources in each vertical level. For other types of frequently used point source (e.g., river discharge), ROMS provides two options to add them into a grid cell: LuvSrc or LwSrc. LuvSrc prescribes the point source as horizontal mass fluxes, while LwSrc prescribes the point source as vertical convergence/divergence. Similarly, the simplest method to add the plume-driven entrainment/outflow is to prescribe them as horizontal mass flux from a nearby ocean grid (H_{Mass}), which takes advantage of the existing framework of LuvSrc. When H_{Mass} is activated, the horizontal velocity from glacier to ocean is determined by

$$u(k) = \frac{1}{\text{d}y\text{d}z(k)} [-q_E(k) + q_D(k)], \text{ or}$$

$$v(k) = \frac{1}{\text{d}x\text{d}z(k)} [-q_E(k) + q_D(k)]$$
(8)

where q_E and q_D are total entrainment and outflow volume fluxes into/out of a ROMS grid cell predicted by BPT and the outflow parameterization; dx, dy, and dz are length dimensions of the ocean grid; k is the grid cell index in vertical direction

In the second method, the point source is prescribed as vertical mass fluxes (V_{Mass}), which is implemented as an increment in vertical velocity

$$\Delta w(k) = \frac{1}{A} \sum_{i=1}^{k} -q_E(i) + q_D(i)$$
 (9)

where A = dxdy is the area of the grid. In ROMS this is equivalent to adding convergence/divergence in an ocean grid. This is the default method to add point sources in MITgcm, and is adopted by Cowton et al. (2015) and other model studies (Bao & Moffat, 2023; Cowton et al., 2015; Hager et al., 2022; Slater et al., 2017) to couple the buoyant plume model with the ocean model. The tracer fluxes F_T of active and passive tracers are independent of the choices of H_{Mass} or V_{Mass}

$$F_T(k) = \frac{1}{4} [-q_E(k)T_{Am}(k) + q_D(k)T_P]$$
 (10)

where $T_{\rm Am}$ and $T_{\rm P}$ are tracer concentrations of the ambient water and plume water, respectively.

The third method Mix, unlike H_{Mass} or V_{Mass} , does not add horizontal or vertical mass fluxes to the ocean grid. This method is newly developed to process the large values of plume-driven convergence and divergence in V_{Mass} , which can generate instabilities in numerical implementations. Subglacial discharge overturns deep, high density water to shallower depths and releases them as a uniform water mass (Mankoff et al., 2016); as a result, the isopycnals near the neutral buoyant depth Z_p are stretched to reflect the overturning of deep water. The distorted isopycnals generate baroclinic pressure gradient and drives the exchange flow, forming an outflowing plume similar to V_{Mass} . Without adding mass or tracer fluxes, Mix calculates the expanding/shrinking of isopycnals internally; then the new profiles of tracers are rewritten back into the ocean grid before the execution of baroclinic timestep to mimic the distortion in isopycnals.

In Mix, we consider each grid cell is a rectangular box of volume $vol^0(k) = A \cdot dz(k)$ and uniform tracer concentration $T^0(k)$. Each grid cell is allowed to expand/contract and modify its tracer concentration based on the volume and tracer flux into or out of the cell by entrainment q_E and outflow q_D (Figure 2). Note that the expansion/contraction of grid cells occurs only in the parameterization algorithm and not in the ROMS grid. Integrating over one baroclinic timestep Δt , the volume and tracer concentration for each level become

WANG ET AL. 6 of 21

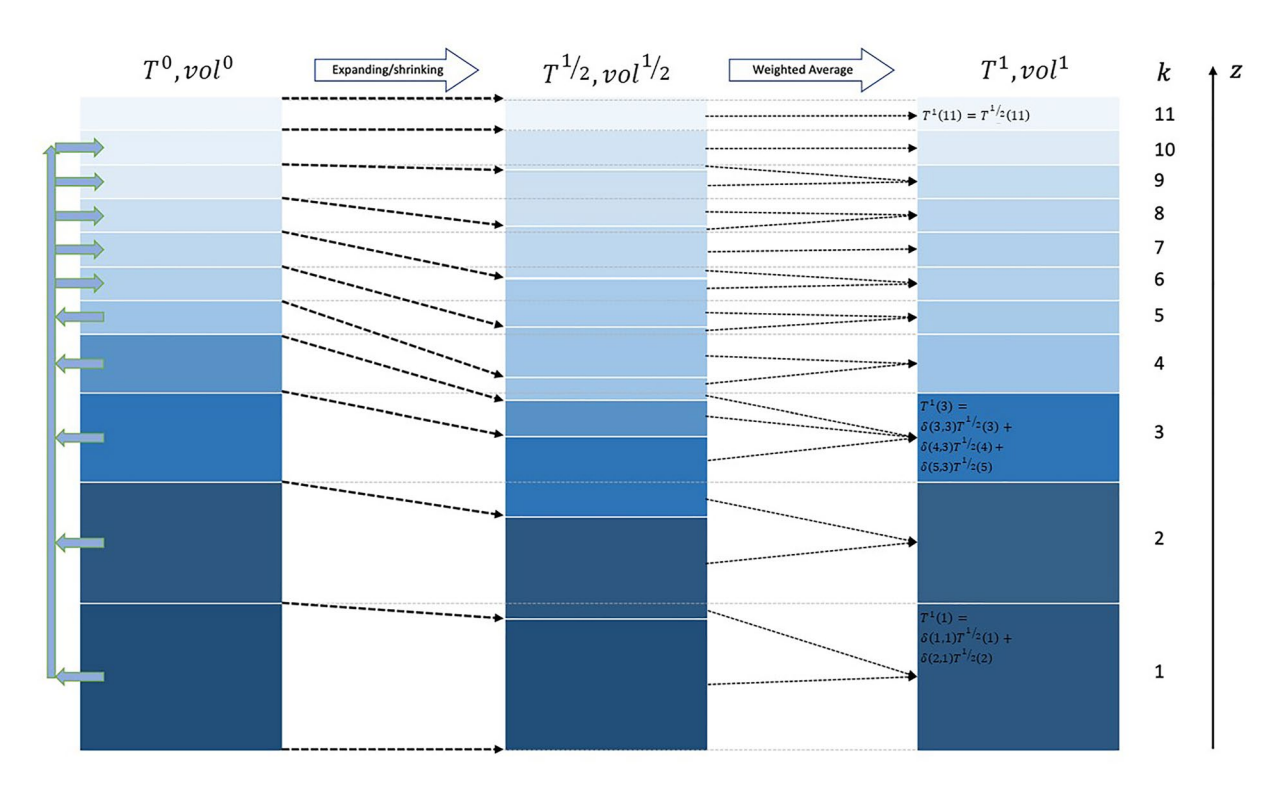


Figure 2. Schematics of the Mix coupling method. From left to right are the states of box volumes and tracer concentrations at step 0, 1/2 and 1, respectively. The colors denote the concentration of tracers (e.g., salinity, temperature and passive tracers) before/after each step of calculation. Blue arrows on the left side denote mass transports driven by the subglacial discharge plume; the arrows from step 0 to 1/2 denote the direction of isopycnal movement in response to box expansion/contraction; the arrows from step 1/2 to 1 denote the weight averaging process to recalculate tracer concentrations in the original grid space.

$$\operatorname{vol}^{1/2}(k) = \operatorname{vol}^{0}(k) + \Delta t [-q_{E}(k) + q_{D}(k)]$$

$$T^{1/2}(k) = \frac{\left[\operatorname{vol}^{0}(k) - \Delta t q_{E}(k)\right] T^{0}(k) + \Delta t q_{D}(k) T_{P}}{\operatorname{vol}^{1/2}(k)}$$
(11)

The superscript 1/2 denotes that this is merely an intermediate step. After this step the vertical grid spacing is distorted, and a transformation is required to project the new profile back to the original grid space (Figure 2). This is achieved by weighted averaging

$$T^{1}(k) = \sum_{i=1}^{N} \delta(i, k) T^{i/2}(i)$$
(12)

where $0 = \delta \le 1$ is the weight function of each level to transform from the intermediate to original grid space. The value of δ is 0 where the intermediate grid does not overlap with the original grid and is between 0 and 1 if the two partially overlap. After the transformation, tracer concentration profile is rewritten back into the ocean model, without introducing any momentum into the grid cells.

In a hydrostatic GCM like ROMS, Mix and V_{Mass} produce very similar solutions (see Section 3.2). The advantage of Mix over V_{Mass} is that it is numerically more stable and can tolerate much larger baroclinic timesteps. Implementation of Mix is effectively a lock-exchange release and drives the same baroclinic flows as the other two schemes, but has zero barotropic transport. Since the baroclinic exchange tends to be an order of magnitude larger than the barotropic transport, its neglect will have negligible impact on the solution, although how the neglect of this weak barotropic transport will manifest in the long term is uncertain.

In ROMS, the options LuvSrc (used in H_{Mass}) and LwSrc (used in V_{Mass}) are generally used to represent rivers in estuarine and coastal simulations. For rivers, fluxes of freshwater are prescribed as a uniform flow in both depth and cross channel direction from one end of a narrow river channel, in which case LuvSrc and LwSrc produce similar results. Subglacial discharge, on the other hand, drives strong baroclinic circulation in the near field. The

WANG ET AL. 7 of 21

barotropic signal is relatively weak, and the prescribed fluxes are associated with significant shear. As a result, H_{Mass} , V_{Mass} and Mix are expected to produce very different results due to the way that initial shear is prescribed. Moreover, subglacial discharge drains into fjords through channels of ~100 m width (e.g., Jackson et al., 2017; Rignot et al., 2015), while the width of glacier front is on the order of 1–10 km.

2.3. ROMS Implementation

The simulations in this study are carried out with the ROMS-ICEPLUME coupled modeling system (https://github.com/ChuningWang/roms-iceplume). Since this is the first time the outflow parameterization and couplers are implemented and tested in ROMS, we briefly describe the detailed configuration and implementing procedure.

First, the upwelling parameterization (BPT) calculates the physical properties of the buoyant plume based on the subglacial discharge flux, plume geometry, fjord stratification, and terminates upwelling when the plume's vertical momentum becomes zero, defined as depth Z_T . Second, the neutral buoyant depth Z_P is determined as the core depth of outflowing plume. This is achieved by searching downward from Z_T until the density of plume water is smaller than that of ambient water.

The density profile of ambient water is determined by averaging over a small "box" of $m \times n$ grids near the subglacial discharge source. The values of m and n are arbitrary and are defined in model input files. The reason to use a regional average instead of only the adjacent grid is to avoid strong fluctuations caused by the convective plume itself. A demonstration of the effect of averaging is shown in Supporting Information S1.

We choose horizontal resolution to be equal or slightly larger than the maximum l_m over the course of the simulation. Since l_m is either predefined as a model input or computed by BPT, setting the grid size to the maximum l_m allows the inflow and outflow to be prescribed to a single horizontal grid. Higher resolution runs would allow the outflow to span over several horizontal grids. However, numerical tests (not shown) suggest that using horizontal resolution higher than l_m does not greatly alter the near field circulation structure.

This plume model can be reverted to Cowton et al. (2015) by turning off the outflow parameterization and using V_{Mass} or Mix. When the outflow parameterization is turned off, the upwelling algorithm terminates when Z_p is determined and all outflow volume goes into the single layer near Z_p . To increase model flexibility, we give the option to turn the outflow parameterization on (hereinafter OP) or off (hereinafter NOP) for each coupler option. By combining OP/NOP with $H_{Mass}/V_{Mass}/Mix$, six outflow/coupling methods are available.

2.4. Numerical Experiments

Three groups of experiments are carried out to test the model framework. The first group (Ex 1) uses a 2-D setup, aiming to demonstrate the outflow parameterization and to produce an outflow best resembling the tank experiments of Ching et al. (1993). All 6 model configurations are tested in Ex 1; for simplicity, only the results of H_{Mass}/OP are reported here. The grid is oriented in X-Z direction; horizontally, the spatial resolution dx is uniformly 300 m, and the total length of model domain is 30 km. Depth is uniformly 200 m with 40 vertical layers, with increased vertical resolution in the top 100 m. Initially the salinity is stratified in two-layers; the lower layer (below 50 m) salinity S_0 is fixed to 35 PSU, and a variety of surface salinities S_1 = 5, 15, 30, 33, 34 PSU are used to produce variation in background stratification. Vertical salinity structure across the halocline is represented by a hyperbolic tangent function. Subglacial discharge is added from the bottom of water column (200 m) at x = 0, and the other end (x = 30 km) an open boundary condition is used to allow the plume to exit the domain. A range of subglacial discharge values Q_0 = 10, 25, 50, 100 m³/s are used as another parameter to modify the Richardson number Ri. In total 24 experiments are carried out, which corresponds to Ri values ranging from 0.245 to 15.612.

The second group of experiments (Ex 2) extends the simulation to 3-D to demonstrate the direct influence of the outflow parameterization and coupling methods on the near field circulation. The six outflow/coupling methods (H_{Mass}/OP , H_{Mass}/OP , V_{Mass}/OP , V_{Mas

For the stability (dt) tests, the fjord is represented by a $6,000 \times 4,500 \times 260$ m basin, with 40 vertical layers intensified in the top 100 m. The channel is oriented in east-west direction, with the glacier located on the west

WANG ET AL. 8 of 21

boundary. Horizontal resolution in along/cross channel direction is 200/300 m, respectively. Subglacial discharge is added from a single grid near the glacier centerline; initial discharge is kept constant (200 m³/s) during the simulation. Initially the ambient water is stratified in two-layers similar to Ex 1, with surface salinity fixed to 33 PSU. For the sensitivity (dx) tests, the model domain is extended to 12,000 × 4,500 × 260 m to allow simulations of coarser resolution (up to 600 m); all other conditions are kept the same.

Lastly, a large grid, fjord scale setup (Ex 3) is designed to test the model performance in quasi-realistic conditions. In order to validate the model's performance, the glacial geometry, initial and boundary conditions are configured based on data of in-situ hydrographic and acoustic measurements (Fried et al., 2015; Jackson et al., 2017), and modeled velocity fields are compared with velocity measurements acquired from the same survey. The fjord is simplified as a rectangular basin of 60 km by 4.18 km by 400 m with 40 vertical layers, intensified in the top 100 m; horizontal resolution is uniformly 300 by 220 m inside the fjord. Outside the fjord is a uniform shelf of 139 by 48 km, with resolution linearly decreasing from 350 by 220 m-2,800 by 1,470 m. To prevent the buoyant plume recirculating around the fjord mouth, a southward coastal current of 1 cm/s is prescribed to remove the buoyant plume exiting the fjord. To suppress instabilities generated in the shelf region, the east offshore boundary is closed, stabilizing the coastal current in north/south direction. The length, width and depth of the rectangular basin largely represents dimensions of the Kangerlussuup Sermia (KS) fjord and glacier system in Uummannaq Bay of west Greenland, where near glacier hydrographic measurements were carried out as part of a 3-year field survey (Bartholomaus et al., 2016; Jackson et al., 2017). Initial salinity and temperature profiles are prescribed using these hydrographic surveys, which resembles a typical summer condition in Greenlandic fjords. These simulations provide an opportunity to assess the efficacy of these parameterizations by direct comparison between modeled velocity fields and velocity data obtained from shipboard surveys of the near-field plume in KS fjord (Jackson et al., 2017), which includes 11 repeated cross sections of plume structure.

This final set of simulations is spun-up for 200 days without subglacial discharge; after 200 days subglacial discharge is released at 260 m depth and slowly ramped up to 200 m³/s within 10 days. The glacier grounding line depth is measured by multibeam sonar and reported in Fried et al. (2015) (the glacier terminus depth at the "prow" position); the subglacial discharge rate is given by Jackson et al. (2017), where the discharge rate is estimated inversely using the plume's volume flux and salinity at its outflowing stage. After the spin-up period, the simulation continues for 300 days. The last 200 days of model outputs are averaged as the "steady state" condition. Based on the test results of Ex 2, only two outflow/coupler methods, H_{Mass}/OP and Mix/NOP, are tested in Ex 3.

For the above simulations, the upwelling plume is parameterized using BPT with a finite-line geometry for the plume (Jackson et al., 2017; Jenkins, 2011). Within the ROMS domain, vertical mixing is parameterized using the k- ϵ closure scheme (Warner et al., 2005); horizontally a grid-scaled harmonic viscosity is used to suppress grid-scale noise. The MPDATA (Smolarkiewicz & Margolin, 1998) advection scheme is used to guarantee tracer positivity. To track the trajectory of outflow, dye is released into the subglacial discharge to mark the buoyant plume.

3. Results

3.1. 2-D Simulation

In this section, we focus on the 2-D simulation (Ex 1) carried out with outflow/coupler method H_{Mass}/OP . Figure 3 shows snapshots of the outflowing plume in the first 12 hr of one single simulation ($Q_0 = 50 \text{ m}^3/\text{s}$, $S_1 = 33 \text{ PSU}$). Once the simulation initiates, the buoyant plume forces downstream outflow around the pycnocline (50 m), and the outflow is compensated by inflows from both above and below. Since the plume is a uniform water mass, it generates density anomalies of opposite signs near the pycnocline, which travels downstream with the plume. The negative density anomaly, however, propagates faster than the positive anomaly. It travels downstream with internal wave speed $C_p = \sqrt{g' \frac{H_1 H_2}{H_1 + H_2}}$, in which H_1 and H_2 are layer thicknesses separated by Z_p (Figure 3). This suggests the plume excites a "bow wake" propagating ahead of the outflow.

Since the outflow parameterization is strongly dependent on the Richardson number Ri defined by Equation 1, the outflow structure is expected to vary with respect to both Q_0 and S_1 . Figure 4 shows the modeled outflow at hour 12 in all simulations. At high Ri values (Ri > 1.6), the outflow is almost strictly below the pycnocline, which is compensated by a deep return flow. The strong density jump prevents the plume water from mixing with the

WANG ET AL. 9 of 21

21699291, 2023, 8, Downloaded from https://agupubs.onlinelibrary.wiley.com/doi/10.1029/2023JC019924 by Rutgers University Libraries, Wiley Online Library on [27/08/2025]. See the Terms

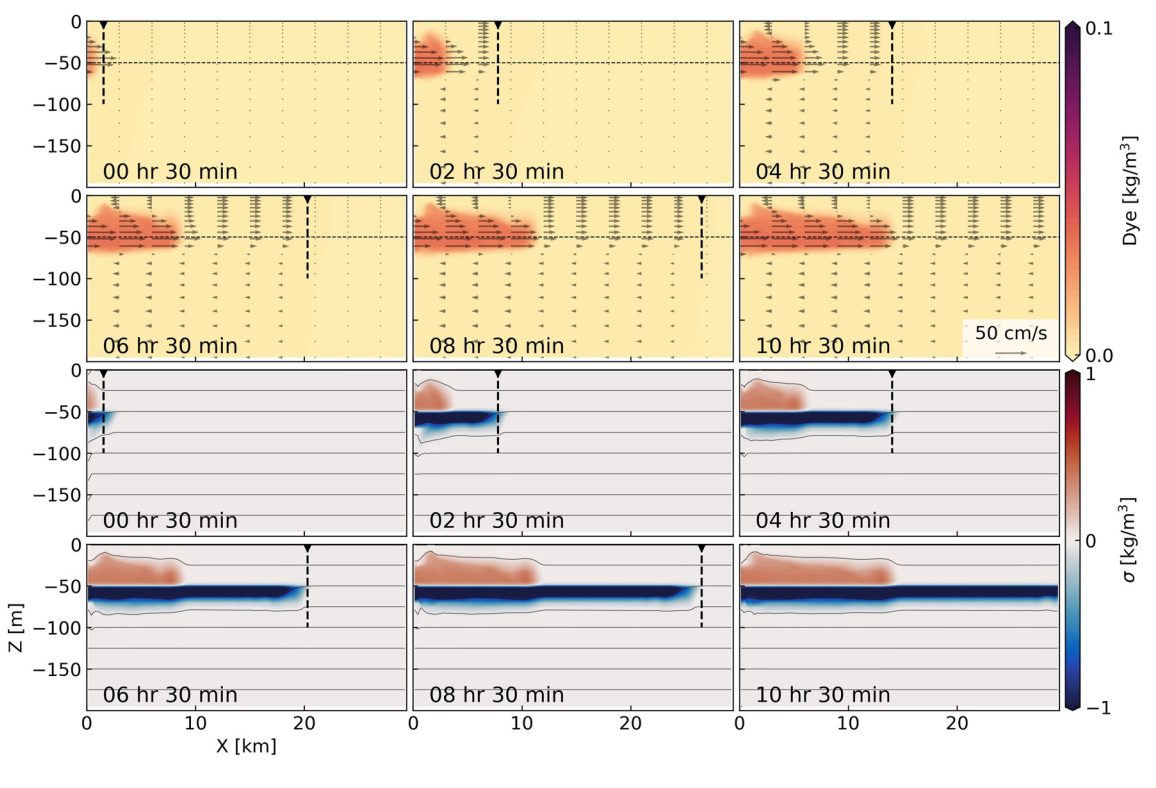


Figure 3. Development of the outflowing plume in Ex 1 during the first 10.5 hr, modeled with method H_{Mass}/OP. Upper panels are subglacial discharge dye concentrations (color) and velocities (vector); lower panels are density (contour) and its anomality from initial condition (color). Initially the contour lines are evenly spaced of 25 m intervals. Triangles and dash lines mark the theoretical position of signal travels with internal wave speed.

top layer, and very little momentum penetrates across the pycnocline. In some cases (e.g., $Q = 100 \text{ m}^3/\text{s}$, $S_1 = 5 \text{ PSU}$), a separate circulation develops in the top layer only, but is spatially variable and is not well correlated with the main outflow. At intermediate Ri values (0.4 < Ri < 1.6), the outflow partly penetrates into the top layer, and return flows are generated both above and below. One exception is $S_1 = 34 \text{ PSU}$ and $Q_0 = 25 \text{ m}^3/\text{s}$, in which case the stratification is too weak, and the plume quickly mixes with the top layer, thus the surface return flow is not identifiable. When Ri is small (Ri < 0.4), the upwelling plume penetrates fully into the top layer, and a surface outflow is formed. In this case, the major pycnocline is the base of the plume instead of the original density jump. Therefore, the actual Ri is defined using the density difference between plume and ambient water, which is higher than the background stratification.

The modeled outflow structure, as a function of Ri, well reflects the parameterization of Ching et al. (1993). The modeled subglacial dye distribution well resembles that of the tank experiments, and so does the velocity profiles. When applied to a continuously stratified condition, the parameterization is also able to generate an outflow structure well resembling the laboratory observations of Baines (2002) (not shown), which is carried out in conditions of constant N^2 . This suggests that this outflow parameterization is applicable in continuously stratified water, despite the two-layer fluid assumption.

Similar experiments are also carried out using the Mix/NOP parameterization. In general, Mix/NOP produces similar results in terms of baroclinic flow structure, thus they are not reported here. The primary differences occur in 3-D simulations, which will be reported in the following two sections.

3.2. 3-D Small Grid Simulation

In this section we focus on the 3-D structure of the outflow in the near field within \sim 5 km from glacier front based on a suite of simulations in the Ex 2 grid. In later sections we will briefly show and discuss the evolving plume as it travels further downstream where it develops a regime similar to a coastal current.

The velocity fields at 50 m, which is the pycnocline and outflow core depth, after one model day are shown in Figure 5 to demonstrate the initial pathway of outflowing plume. In general, H_{Mass} produces a jet-like flow with strong

WANG ET AL. 10 of 21

21699291, 2023, 8, Down

from https://agupubs.onlinelibrary.wiley.com/doi/10.1029/2023JC019924 by Rutgers University Libraries, Wiley Online Library on [27/08/2025]. See the Terms

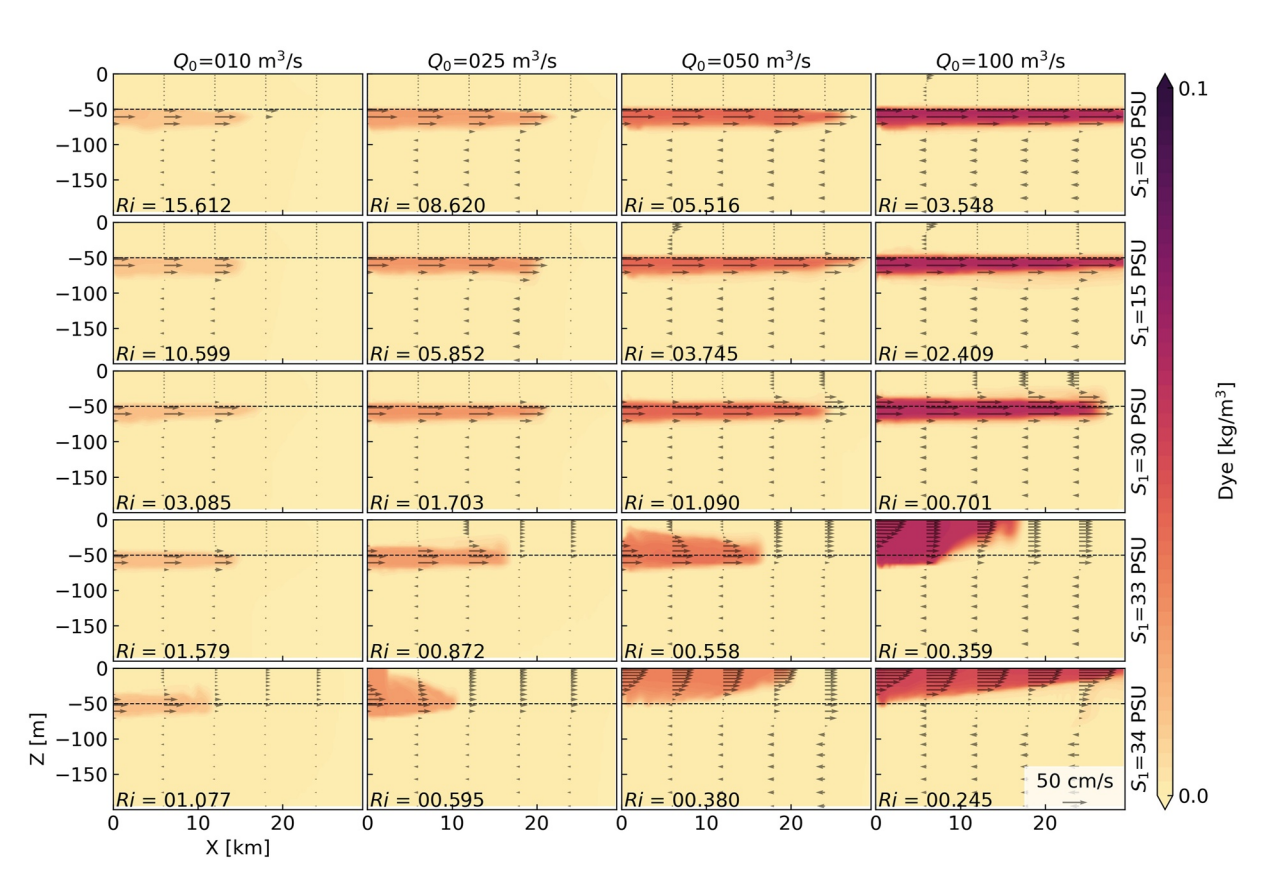


Figure 4. Along-channel distribution of subglacial discharge dye concentration (color) and velocity (vector) in Ex 1 at hour 12. Horizontally the plots are aligned with respect to subglacial discharge Q_0 ; vertically the plots are aligned with respect to surface layer salinity S_1 . The Richardson Number value of each experiment is given in the bottom-left corner.

momentum in the along channel direction, which is quickly diverted to the south boundary under influence of the Coriolis force. Without the outflow parameterization, H_{Mass} /NOP drives a strong outflow that occupies the top 150 m in the near field (Figure S4 in Supporting Information S1). This is a result of vertical mixing driven by strong shear generated in the near field without the outflow parameterization, highlighting the importance of the OP treatment.

On the other hand, V_{Mass} and Mix produce an outflow that initially spreads laterally and fills the width of the domain within 2 km from the glacier. Further downstream the Coriolis force diverts the flow to the south wall, forming a coastal current. Overall, the flow structure is significantly different from that of H_{Mass} . However, solutions of V_{Mass} and Mix are less sensitive to the outflow parameterization than H_{Mass} . When numerically stable, V_{Mass}/OP , V_{Mass}/OP ,

In terms of numerical stability, in general Mix is the most stable among the three coupling methods, while V_{Mass} requires the shortest time step. At dt = 5 s, even though V_{Mass}/NOP still produces solution of a surface plume, a detailed examination shows vertical fluxes have violated the CFL condition and the solution will soon diverge. Similarly, the solution of V_{Mass}/OP begins to diverge at dt = 10 s and produces slightly different results in the near field. Overall, the two most promising method for further applications are prescribing the horizontal velocities with the outflow parameterization (H_{Mass}/OP) and the release of mixed fluid without the outflow parameterization (Mix/NOP). Applying horizontal velocities without the outflowing parameterization (H_{Mass}/NOP) forces unrealistic vertical shear overestimate mixing, while prescribing vertical velocities with or without the OP (V_{Mass}/OP , V_{Mass}/NOP) produce similar results to Mix/NOP, even though they are numerically less stable. Similarly, Mix/OP produce similar solutions to Mix/NOP but is also numerically less stable.

Then the outflow/coupling methods are tested with respect to along channel grid resolution. Since H_{Mass}/OP and Mix/NOP are the two best performing methods, only the results of these two are shown in Figure 6. The comparison suggests that in general, model performance of H_{Mass}/OP is less sensitive to dx. At the highest resolution (dx = 100 m), the velocity fields modeled by H_{Mass}/OP and Mix/NOP show more resemblance to each other, and

WANG ET AL. 11 of 21

21699291, 2023, 8, Downlo

from https://agupubs.onlinelibrary.wiley.com/doi/10.1029/2023JC019924 by Rutgers University Libraries, Wiley Online Library on [27/08/2025]. See the Terms

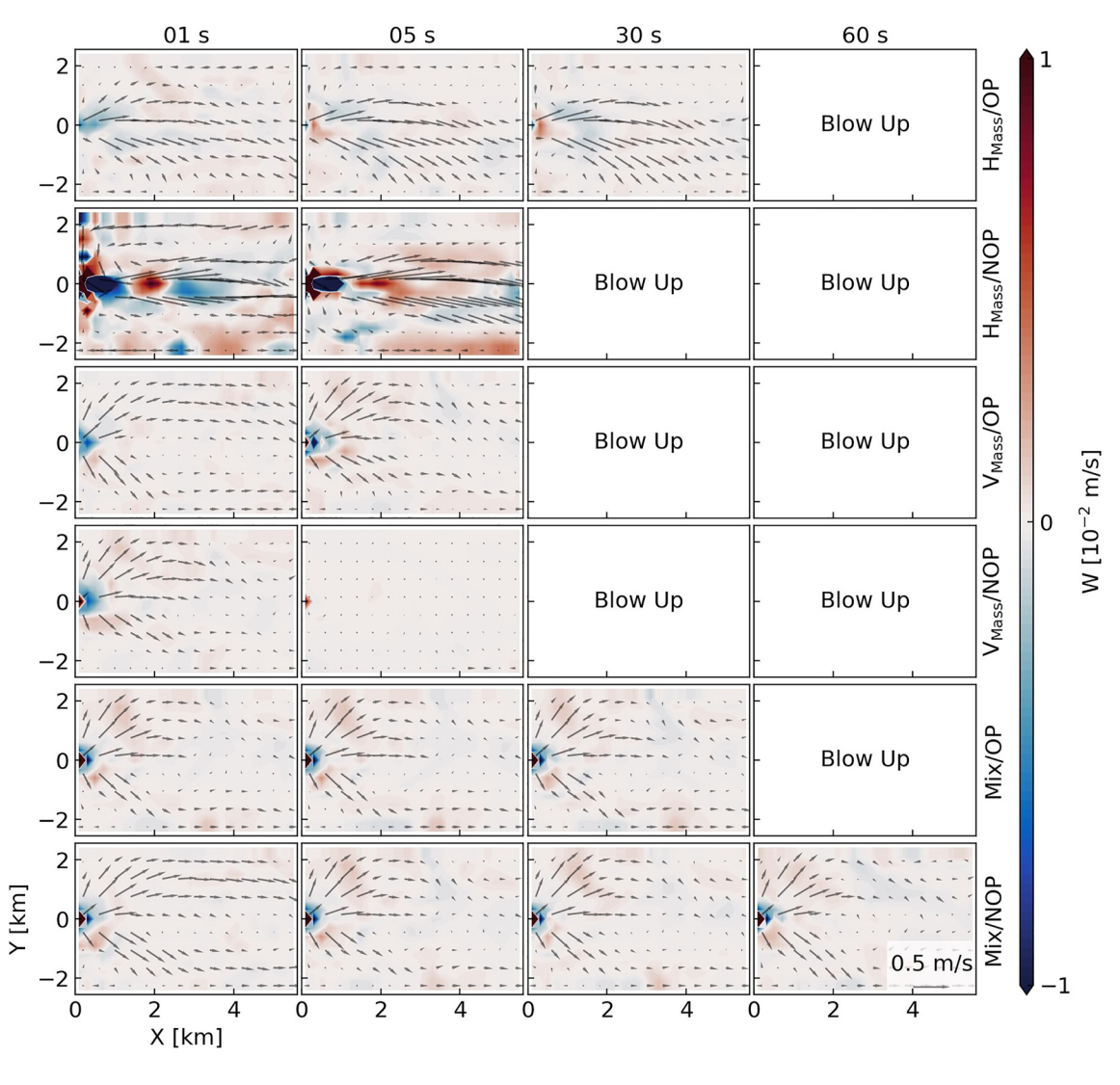


Figure 5. Modeled velocity field (vector: u/v, color: w) at 50 m in Ex 2. Horizontally the plots are aligned with respect to baroclinic time step lengths (dt); vertically the plots are aligned with respect to outflow parameterization and coupling methods.

in both cases subglacial dye does not reach the northern boundary. As dx increases, the solution begins to diverge for H_{Mass}/OP and Mix/NOP. At the coarsest resolution (dx = 600 m), H_{Mass}/OP produces solutions very similar to the high-resolution cases in velocity fields; in addition, the main path of the plume, which is marked by the 0.02 contour in dye concentration, does not change significantly from high resolution cases. On the other hand, in Mix/NOP, as dx increases, the plume tends to spread in cross channel direction with a bifurcating structure. Subglacial dye reaches the north boundary, in contrast to the highest resolution case; at the lower resolution the plume structure bifurcates more strongly causing rapid lateral spreading of the dye. Note that this bifurcation is largely absent in the simulations forced with the H_{Mass} parameterization. A similar bifurcation that Mix/NOP produces is also evident in the near field in Figures 2b and 2c in Carroll et al. (2017). In summary, the parameterization that prescribes the horizontal velocity and parameterizes the outflow physics (H_{Mass}/OP) is less sensitive to grid resolution than the parameterization that releases mixed fluid into the domain and does not include an outflow parameterization (Mix/NOP).

In addition to the difference of flow structure between H_{Mass} and V_{Mass}/Mix , the importance of the newly employed outflow parameterization OP should also be highlighted. In Figure 5, it is shown that without OP, H_{Mass}/NOP overestimates the velocity of outflow at the outflowing depth, and one consequence is that the strong shear produces excessive and unrealistic vertical mixing and increases the overall volume exchange. To further demonstrate the necessity of OP, the profiles of down-fjord and vertical velocities u/w, vertical diffusion coefficient K_s , turbulent kinetic energy $TKE = q^2$ are averaged over the model domain and shown in Figure 7. The strong outflow generated

WANG ET AL. 12 of 21

21699291, 2023, 8, Downloaded from https://agupubs.onlinelibrary.wiley.com/doi/10.1029/2023JC019924 by Rutgers University Libraries, Wiley Online I

and-conditions) on Wiley Online Library for rules of use; OA articles are governed by the applicable Creat

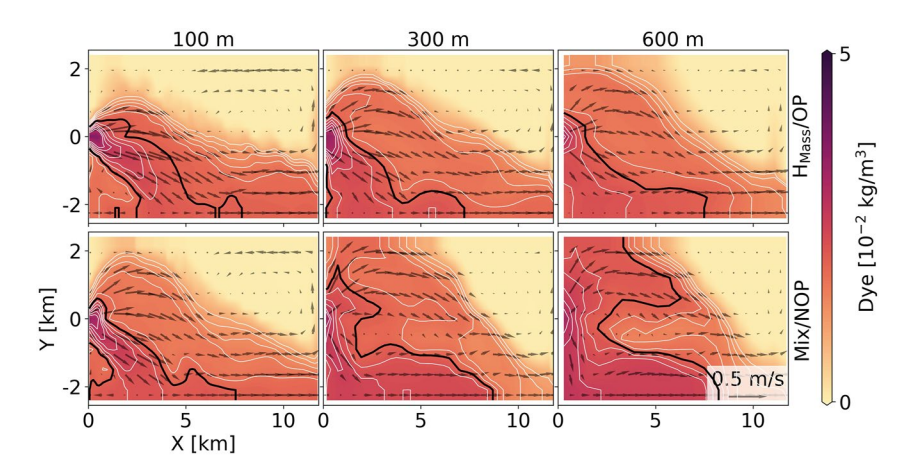


Figure 6. Modeled velocity fields (vector) and subglacial discharge dye concentration (color) at 50 m depth. Dye concentration is contoured in 0.002 kg/m^3 increments (white), with the contour of 0.02 kg/m^3 highlighted in black. Horizontally the plots are aligned with respect to grid resolution in along channel direction (dx); vertically the plots are aligned with respect to outflow parameterization and coupling methods.

by H_{Mass}/NOP does not only occurs at the outflowing depth 50 m, but also extends to over 100 m in the water column. In H_{Mass}/NOP , the large outflowing velocity coming from a single layer generates excessive mixing at the head of glacier terminus, with vertical diffusion coefficient 2–3 magnitudes greater than other model configurations (Figures 7c and 7d). The excessive mixing drives greater volume exchange in the down-fjord direction, and also initiates stronger vertical transports to balance the increasing horizontal volume flux (Figures 7a and 7b).

Another disadvantage of not using the outflow parameterization is that the solution will be more sensitive to vertical grid resolution. In H_{Mass}/NOP , since the outflow ejects at a single layer, the thickness of that layer sets

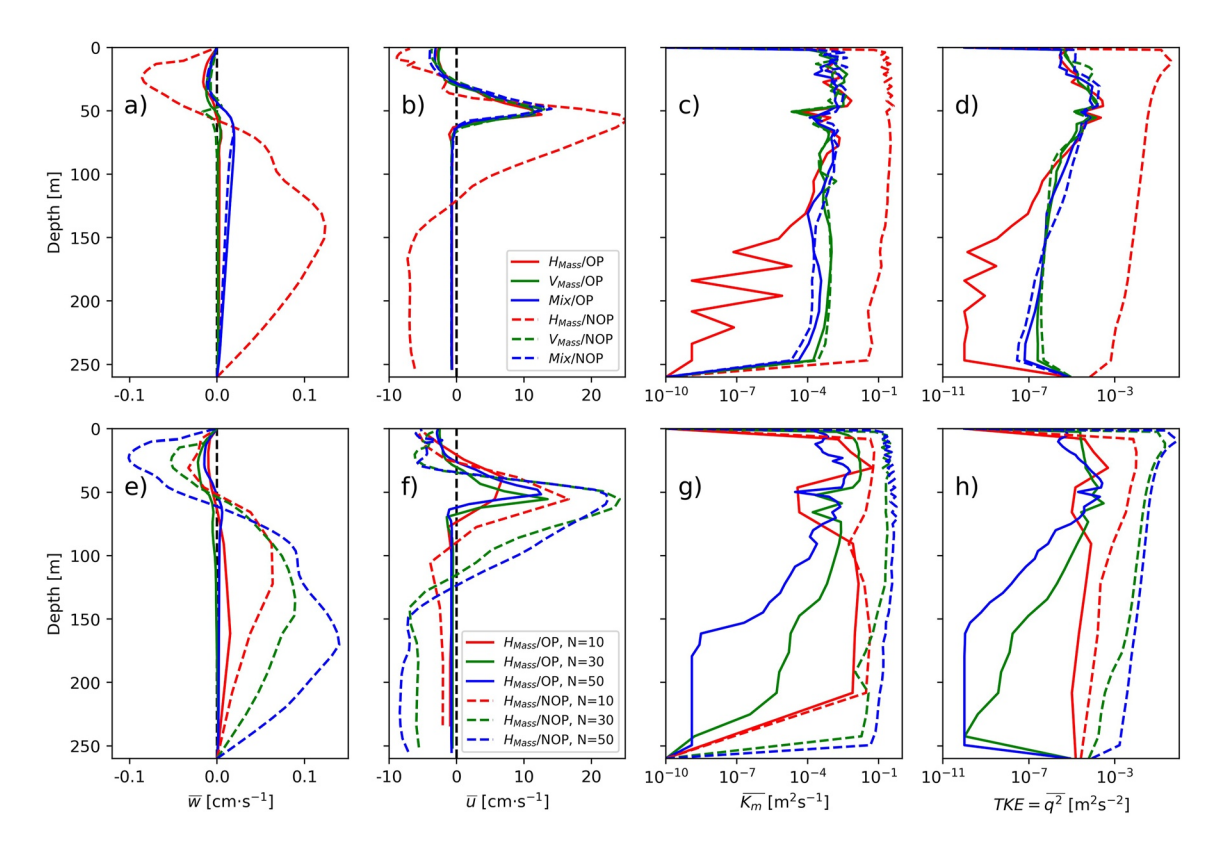


Figure 7. Vertical profiles of vertical velocity, down-fjord velocity, diffusion coefficient and TKE, averaged over the model domain at hour 24. (a–d) Experiments of different parameterization methods. (e–h) Experiments of different vertical grid levels, from two parameterization methods H_{Mass}/NOP and H_{Mass}/OP.

WANG ET AL. 13 of 21

the initial velocity and thus the mixing intensity in the adjacent grid cell. To test the model sensitivity to vertical resolution, extra experiments are performed following the configuration of Ex 2. As the total number of model σ layers decreases from N=50 to N=10, the velocity and thickness of outflowing layer both decrease (Figure 7f) and the maximum volume exchange reduces from $\sim 10 \times 10^4$ m³ s⁻¹ to $\sim 3 \times 10^4$ m³ s⁻¹ in H_{Mass}/NOP, while in H_{Mass}/OP the maximum volume exchange is relatively stable at $\sim 1.2 \times 10^4$ m³ s⁻¹ and only increase to $\sim 2.0 \times 10^4$ m³ s⁻¹ at N=10 (not shown) due to a thicker outflow layer at very low resolution.

Based on the above simulation results, we conclude that: (a) Without the outflow parameterization, H_{Mass} produces an unrealistic solution and is numerically the least stable coupling option; Mix and V_{Mass} produce very similar solutions, but Mix is preferred because of its superior numerical stability. (b) When the outflow parameterization is implemented, the solution and numerical stability of H_{Mass} are both greatly improved. For the above reasons, it can be concluded that H_{Mass}/OP and Mix/NOP are the two most advantageous model configurations, and thus are carried into the numerical simulations of Ex3.

3.3. KS Glacier Simulation

In Ex 3 the subglacial discharge is constant after a 10-day ramp up period and in the near field the outflow is relatively steady after the ramp up with little temporal variability. However, in the far-field (\sim 10 km away from glacier front), the downstream velocity shear generates temporal variability (not shown) that we remove by averaging over the last 200 days of the simulation. This eddy-like motion in the far-field is beyond the scope of this work; instead, in this study we focus on the near-field velocity structure driven by subglacial discharge. In addition, we note that simulations presented in Cowton et al. (2015) also exhibited eddying/meandering motions, as does the more recent realistic Greenlandic Fjord simulations of Zhao et al. (2023).

A comparison between models and observation along the major axis of the flow is shown in Figure 8. H_{Mass} /OP reproduced the observed strong outflow that extended from near surface to depth of 50 m and the observed weaker return flow at depth. The outflow in the observations and H_{Mass} /OP is predominantly in the along channel direction and carries strong momentum. Below the strong outflow is a compensatory inflow, extending from 50 to 150 m. In contrast, Mix/NOP does not produce a unidirectional outflowing plume, instead the outflow bifurcates from the point source and travels to both north and south walls of the fjord, while a strong inflow traveling toward glacier is formed in the middle. The outflow extends from near surface to roughly 50 m; the inflow extends deeply to 150 m and decays with depth. Moreover, H_{Mass} /OP captures many aspects of the structure of the flow including the asymmetry of the jet with both the model (Figure 8, color) and data (contour) showing stronger lateral shears on the north side of the jet as well as a weaker outflowing region along the northern wall. While the structure of the modeled return flow at depth deviates somewhat from the data, they both show a subsurface core centered around 60–70 m depth with maximum velocities of ~10 cm/s. The model's flow for H_{Mass} /OP are biased to the north but are considerably more faithful to the observations that Mix/NOP whose return flow occurs at the surface and the bifurcation of the jet is apparent by strong flows on both the north and south walls of the Fjords.

Jackson et al. (2017) calculated the volume flux of outflowing plume by integrating the transport within the 0.03 m/s velocity contour line that encloses the maximum velocity, and reports a mean outflow of $7,200 \pm 500$ m³/s averaged over 8 sections in which the plume structure is prominent. Using the same method (integrating within 0.03 m/s velocity contour, enclosing the plume core for H_{Mass}/OP , or the two plume cores for Mix/NOP), modeled velocity field yields a total outflow volume flux of 8,800 and 10,100 m³/s in H_{Mass}/OP and Mix/NOP, respectively. Both values are on the same order of magnitude with the measurements of Jackson et al. (2017), showing that BPT is able to properly set up the buoyancy-forced exchange flow; this is expected since Jackson et al. (2017) used the outflowing plume's volume flux and the BPT parameterization to inversely estimate the subglacial discharge rate, thus our forward implementation of BPT should result in a similar plume terminus volume flux. Even so, of the two model configurations, H_{Mass}/OP is a much better representation of the observed volume flux, with only a 20% difference, despite the idealized geometry and neglect of local and remote meteorological forcing.

In the middle fjord region, the responses driven by H_{Mass} /OP and Mix/NOP show more similarities compared with the near field (Figure 9). When averaged over along-channel direction between 20 and 40 km, the strong downstream flow is focused on the south wall of the fjord, and the return flow occurs near the north wall (Figures 9c and 9h). The along channel velocity profile (Figures 9b and 9g) shows a three-layer exchange flow, with a strong outflow from roughly 5–50 m, and two return flows above and below the outflow. The top layer (above 5 m) contributes very little to the exchange volume flux, and the outflow is primarily compensated by the inflow at

WANG ET AL. 14 of 21



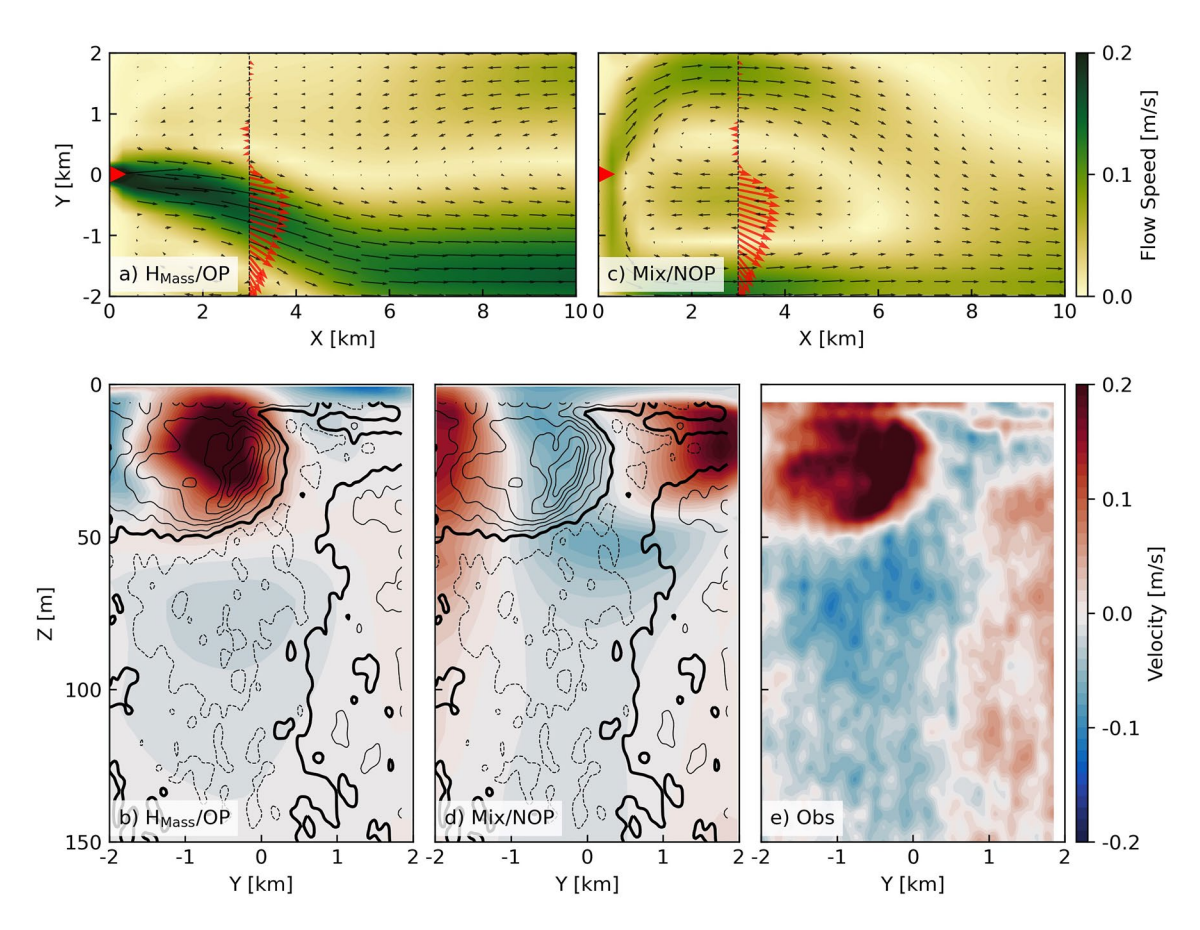


Figure 8. Velocity field modeled by H_{Mass}/OP (a, b) and Mix/NOP (c, d) and from observation $\mathfrak E$ in the near field. (a, c) Velocity averaged over the top 50 m in the near field (0–10 km from glacier). Red vectors are Section 7 of the KS-1 observations. The observations are rotated to align with modeled velocity direction. (b, d) Cross channel sections at 3 km from the glacier, showing component of velocities along principal axis from model (color) and observation (contour). Contour intervals are 0.05 m/s; the thick line marks zero and solid/dashed lines are positive/negative value. (e) Observations of cross channel velocity (Sect 7 of KS-1), same as the contour lines in (b, d).

depth. When traveling downstream, the outflow mixes with fjord water below the plume, and subglacial dye is diffused to deeper depth (Figures 9e and 9j); in both cases subglacial dye mixes to \sim 80 m deep, as indicated by the depth of the 0.01 isoline; H_{Mass}/OP drives stronger mixing, as suggested by overall lower dye concentration in the plume water layer. Below the plume, subglacial dye mixes into the lower inflowing layer and results in a recirculation of plume water. Since subsurface mixing is more prominent in H_{Mass}/OP , the outflowing plume mixes more with the layer below, which results in a greater positive temperature anomaly compared Mix/NOP.

The outflowing plume (Figures 9b, 9c, 9g, and 9h) in H_{Mass}/OP extends deeper than Mix/NOP; near the south wall, the outflow expands to 80 m in H_{Mass}/OP (compared with 60 m in Mix/NOP). On contrary, maximum outflow speed is found at 14 m in H_{Mass}/OP , which compared with Mix/NOP (18 m) is slightly shallower. In addition, below the outflow, a much stronger return flow is formed in H_{Mass}/OP , which suggests that more mixing is generated and stronger exchange flow is established. In the middle fjord section, the integrated outflow volume fluxes are 9,700 and 6,900 m³/s in H_{Mass}/OP and Mix/NOP, respectively.

Overall, in the near field, the model configuration H_{Mass}/OP produces outflow better resembling the observation. In the middle fjord, the along channel flow structure show more similarity in the two setups; H_{Mass}/OP generates more mixing at subsurface, which results in stronger exchange flow and greater downstream volume flux.

4. Discussion

Using in-situ observations from a tidewater glacier fjord, we have demonstrated that ROMS-ICEPLUME is able to reproduce the structure of an outflowing plume generated by subglacial discharge. In the previous section we

WANG ET AL. 15 of 21

21699291, 2023, 8, Downloaded from https://agupubs.onlinelibrary.wiley.com/doi/10.1029/2023JC019924 by Rutgers University Libraries, Wiley Online Library on [27/08/2025]. See the Terms and Conditions

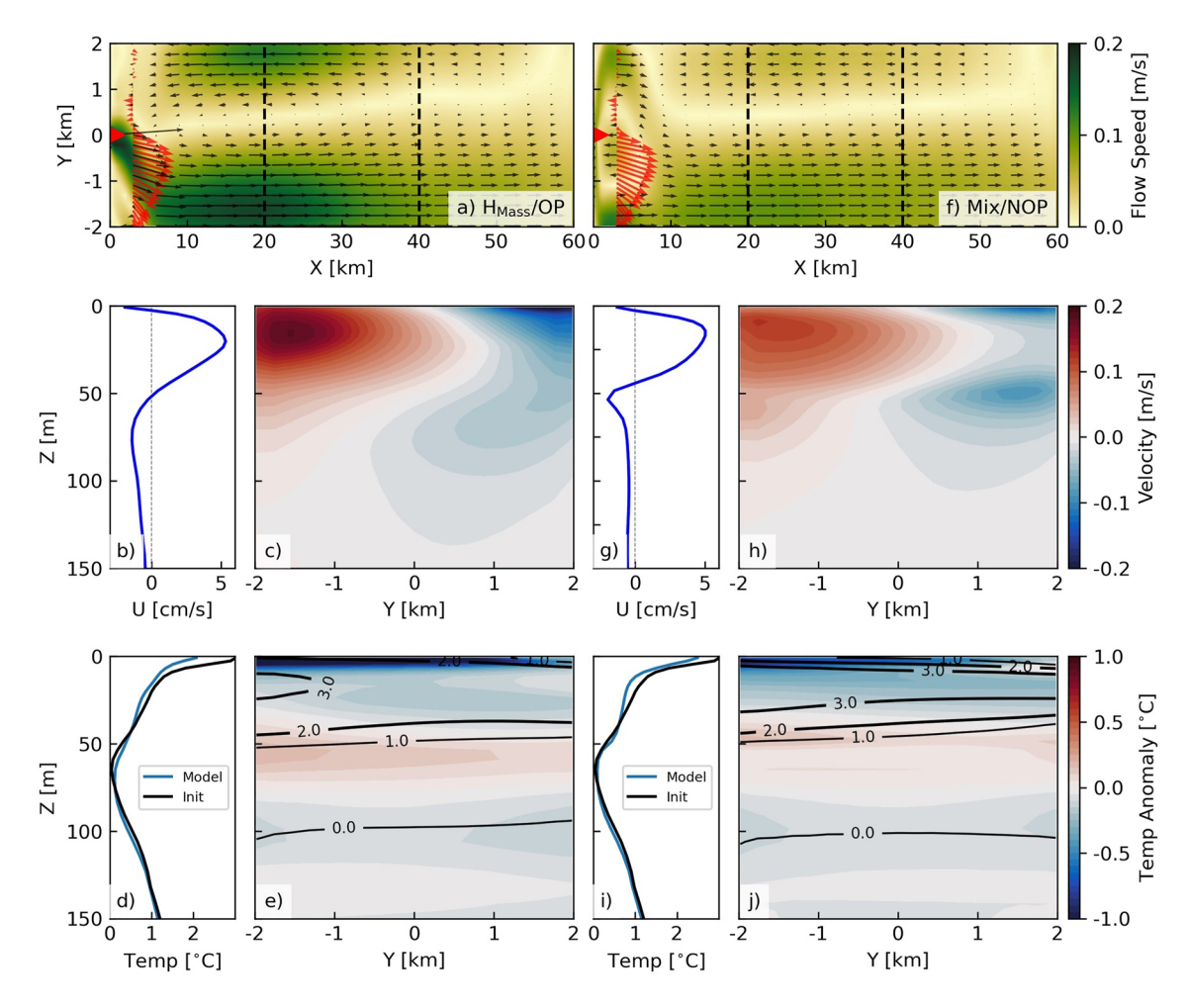


Figure 9. Velocity and tracer fields modeled with H_{Mass}/OP (a–e) and Mix/NOP (f–j) over the entire fjord domain. (a, f) Velocity averaged over the top 50 m, similar to Figure 8, from glacier front to fjord mouth. (b, g) Velocity profiles in along channel direction, averaged over the middle fjord (bounded by dashed lines in a, f). (c, h) Cross channel sections averaged over the middle fjord region, showing component of velocities in along channel direction. (d, i) Temperature profiles averaged over the middle fjord, of initial and modeled states. (e, j) Cross channel sections averaged over the middle fjord, showing temperature anomaly from initial condition (color) and subglacial discharge dye concentration (contour, values have units of 0.01 kg/m³).

have proposed two potentially useful model configurations: H_{Mass} /OP and Mix/NOP. Mix/NOP uses a coupling method similar to previous modeling studies (Cowton et al., 2015), while H_{Mass} /OP implements a new coupling method and additional parameterizations. Both configurations are numerically stable and produce buoyancy driven exchange flow near glacier front.

In the 2-D simulation (Ex 1) the velocity signature of the plume propagates downstream at the internal wave speed (Figure 3). However, there is an asymmetry to the density anomaly, with the lower layer density anomaly propagating at the internal wave speed, while the upper layer density anomaly propagates at closes to half the internal wave speed. This is consistent with observations made in a large freshwater lake in UK, Loch Ness (Farmer, 1978; Thorpe, 1971) whereby wind forced disturbances of the thermocline non-linearly develop into a depression wave, and leading edge of the wave develops into a surge that causes the pycnocline to asymmetrically deepen relative to shoaling when the lower layer is deeper than the upper layer (Thorpe, 1971). While of interest, the details of this non-linear wave dynamics are beyond the scope of this study.

Even though both H_{Mass}/OP and Mix/NOP produce reasonable and similar results in the far field, the forms of circulation in the two simulations are very different particularly in the near-field. H_{Mass}/OP drives a strong jet-like buoyant flow from the point source, which travels predominantly in the along channel direction and follows the south wall; Mix/NOP produces a pure buoyancy-driven gravity current, which spreads in cross channel direction and travels downstream along both walls. In addition to the flow structure, the overall volume transports

WANG ET AL. 16 of 21

estimated by H_{Mass} /OP is also a better representation of field observation, with an overestimation of only 20% compared with Mix/NOP (40%).

Another fundamental difference between H_{Mass}/OP and Mix/NOP is the structure of the flow. In particular Mix/NOP exhibits much more recirculation in the vicinity of the glacier than H_{Mass}/OP. This is to be expected as Mix/NOP is analogous to the classic Rossby adjustment problem where a large fraction of the potential energy remains near an initial pressure discontinuity and manifests as a recirculating eddy. Both our results with Mix/NOP and those of Carroll et al. (2017), who used a similar parametrization as Mix/NOP, show considerable recirculation of the outflow and a flow that bifurcates at the buoyancy source and spreads to both sides of the channel. In addition, both Carroll et al. (2017) and Mix/NOP show a return flow back toward buoyancy source. While both parameterizations evolve to similar solutions in the far field, difference at the near field could alter submarine melt rates since they are strongly influenced by flow velocities in the vicinity of the glacier (Holland & Jenkins, 1999; Jenkins, 2011; Slater et al., 2018; Zhao et al., 2023). Moreover, recent results (Sutherland et al., 2019) indicate that existing parameterizations for submarine melt considerably underestimate the melt rate and thus forthcoming parameterizations of submarine melt are likely to become even more sensitive to near-field flows and thus quite sensitive to the choice of outflow parameterization.

In the far field, both parameterizations exhibited similar flow structure with the outflow along the south wall, an inflow along the north wall and at depth. Interestingly, both also show that dye injected into the domain with the outflow rapidly spread to regions well beyond the outflowing jet. Indeed, dye concentrations (Figure 9) are fairly uniformly spread across the channel in contrast to the velocity field which exhibits significant lateral shear (Jackson et al., 2017, 2022). In addition, there is considerable downward mixing of the dye into the landward flowing lower layer. These results suggest that geochemical tracers introduced by the buoyant plume, such as noble gasses (Beaird et al., 2018), will spread well beyond the outflowing jet.

Finally, we interpret the results and explain why H_{Mass}/OP outperforms Mix/NOP with respect to the observations of Jackson et al. (2017). Considering a strictly vertical glacier front, and subglacial discharge enters the domain with no horizontal momentum. When the buoyant plume terminates to rise and outflows from glacier front, it should spread radially due to the lack of predominant initial horizontal momentum (e.g., Ezhova et al., 2018; e.g., McConnochie et al., 2020). This radial movement of plume is better described by Mix since the coupler Mix does not prescribe any horizontal momentum. A lateral spreading plume has also been observed in lab experiments (e.g., McConnochie et al., 2020) and simulated in numerical models (e.g., Ezhova et al., 2018), which supports the usage of Mix. In Ezhova et al. (2018) it is even shown that the plume tends to spread in the two directions along the glacier front, much like the bifurcated flows in the simulation of Mix/NOP.

However, the disagreements between field observation and Mix/NOP simulation suggests that in this specific environment the Mix parametrization is missing some important processes. In the field observation of Jackson et al. (2017), even though there are variabilities among each transect, the jet-like outflow structure (as shown in Figure 8e) is a consistent feature during the 2-day survey period. Similar jet-like flow structure is also observed in other tidewater glacier fjords (Jackson et al., 2020; Kienholz et al., 2019; Mankoff et al., 2016; Motyka et al., 2013), suggesting a consistent pattern in outflowing subglacial discharge plumes. We suggest that H_{Mass} compares well with the observations, compared to Mix largely due to glacial geometry, and that in other glacial configurations Mix may be more appropriate. For example, consider a glacier front tilted toward the glacier at the bottom and toward the ocean at the surface (often referred to as undercutting), the buoyant plume cannot move freely in the vertical direction and as it upwells it will be redirected by the inclined surface and gain some horizontal momentum. When the plume leaves the glacier front, it already has some horizontal momentum in the direction of the ice tilt, which might promote the formation of a jet-like outflow that is normal to the glacier front. This geometry structure is a previously observed feature in some marine-terminating glaciers, that is, the largest subglacial discharge outlet of KS glacier is undercut by \sim 250 m at its grounding depth (slope of \sim 45° from vertical), while in locations away from the discharge outlet, the glacial calving front is nearly vertical (Figures 2c and 2d in Fried et al., 2015). This geometry configuration, shown conceptually in Figure 10b, could explain why the outflowing plume tends to form a jet-like flow in vicinity of the KS glacier. Furthermore, the upwelling of a subglacial discharge plume entrains ambient warm water into the plume and transports more heat toward the subglacial discharge outlet, which could locally enhance subglacial melting. As a result, undercutting could develop even when the glacial calving front is initially vertical (Figure 10a), which promotes the system to reach a new state as described by Figure 10b.

WANG ET AL. 17 of 21

21699291, 2023, 8, Downloaded from https://agupubs.online1brary.wiley.com/doi/10.1029/2023JC019924 by Rutgers University Libraries, Wiley Online Library on [27/08/2025]. See

Figure 10. Evolution of buoyant plume near a vertical (left) and calved (right) glacier front. The blue boxes denote the location of glacier terminus, while the green arrows denote the flow pattern of the subglacial discharge plume.

It is also important to note that undercutting near subglacial discharge outlets is not a consistent feature for all marine-terminating glaciers. Recent observations of the LeConte Glacier, Alaska found glacial front geometry of persistent overcutting (where the grounding line is seaward of the sea surface) in the vicinity a subglacial discharge outlet (Abib et al., 2023). In this case, the subglacial discharge plume might not be steered by the glacial geometry, and the Mix parameterization could be more appropriate to describe the initial development of an outflowing plume (Figure 10a).

Even though H_{Mass}/OP has greatly improved the modeling skill of plume-driven near-field circulation, due to the sparsity of observation and the chaotic nature of subglacial discharge plume uncertainties remain. One of the major sources of uncertainty is the configuration of the upwelling plume's vertical structure, more specifically the choice of a line style plume versus axisymmetric style plume or other prescribed forms (Jackson et al., 2017). Each plume style predicts a unique entrainment volume flux and tracer concentration, which determines the initial velocity profile near the glacier front. The choice is rather arbitrary, but basic in-situ surveys could provide information to inversely deduce it from several prescribed forms. Hence, the reliability of model configuration depends on the abundance of in-situ measurements in the specific research site, which is a major limitation toward deploying the model in large scale domain of multiple glacial fjord systems. Second, several basic plume model parameters, for instance, the volume flux of subglacial discharge, are difficult to obtain and often inferred from other type of measurements or products. Furthermore, it should be noted that the model-observation comparison is based on a limited 2-day set of surveys from the KS near-glacier region. On the one hand, the setting and data at KS are well-suited for comparison with an idealized model: the dominant signal in the repeat surveys in a single, steady outflowing plume; wind forcing was weak at the time; and an ice mélange was absent (Jackson et al., 2017). Nevertheless, there are undoubtable some signals from external forcing (tides, winds, icebergs, etc.) that contribute to the observed data and complicate the comparison between the observations and an idealized model with only glacier forcing. All these uncertainties could propagate into the model and eventually hinder its performance. This is a more generic challenge for numerical models, but the upwelling and outflowing parameterizations could potentially amplify the uncertainty due to their sensitivities to certain forcings. The purpose of listing these uncertainties is not to shake the reliability of the parameterization; instead, it is to remind future researchers to revisit these topics as our knowledge of subglacial discharge plume advances.

5. Conclusion

In order to better understand subglacial discharge driven flow in tidewater glacier fjords, a new model framework, ROMS-ICEPLUME is developed by coupling the upwelling and outflow parameterizations with a hydrostatic

WANG ET AL. 18 of 21



Acknowledgments

This work was supported by National

Science Foundation Grant OCE-1948777

and Shanghai Frontiers Science Center

of Polar Research. The computation of

this work was supported by the Siyuan-1

cluster provided by the Center for High

Performance Computing at Shanghai Jiao

Tong University and the Cheyenne cluster (https://doi.org/10.5065/D6RX99HX)

provided by NCAR's Computational and

Information Systems Laboratory. We are

very grateful to Tom Cowton and one

comments on this manuscript.

anonymous reviewer for their insightful

Journal of Geophysical Research: Oceans

10.1029/2023JC019924

general circulation model. The model is composed of (a) the general circulation model ROMS, (b) the BPT module adopted from Cowton et al. (2015) and Jenkins (2011), (c) outflow parameterization option OP developed from Ching et al. (1993) and Noh et al. (1992), and (d) one of three coupler options ($H_{Mass}/V_{Mass}/Mix$) to integrate the parameterizations with ROMS.

The outflow parameterization OP uses an empirical function to determine the nose velocity of outflowing plume and distributes the outflow vertically in several model layers. The coupler options provide different schemes to incorporate plume driven momentum/tracer fluxes in model grids: H_{Mass}/V_{Mass} uses horizontal/vertical mass fluxes to prescribe the momentum/tracer fluxes, respectively, while Mix computes the distortion of isopycnals internally and does not add extra momentum fluxes. The performance of outflow parameterization and coupling methods is tested with idealized numerical experiments. Based on the results, we find that without the outflow parameterization, H_{Mass} produces unrealistic solution and is numerically the least stable coupling option; Mix and V_{Mass} produce very similar solutions, but Mix is more advantageous due to its superior numerical stability. When the outflow parameterization is implemented, the solution and numerical stability of H_{Mass} are both greatly improved.

To validate the module, background stratification and subglacial discharge rates measured or inferred from Jackson et al. (2017) are used to setup and force a semi-realistic simulation, and the modeled velocity fields are compared with in-situ measurements of the plume acquired from the same survey. Model/observation comparison suggests that a combination of outflow parameterization OP and coupler H_{Mass} can reproduce the strong outflowing plume in the near field and the inflow at depth. Both OP and H_{Mass} improve the model performance compared with similar model configurations used by previous studies. Due to the sparsity in observation of subglacial discharge plumes, there are still some uncertainties associated with the parameterizations; these uncertainties should be addressed in future observational and modeling studies as our understanding of circulation in tidewater glacier fjords advances.

Data Availability Statement

The numerical simulations in this study are carried out with the open-source software ROMS-ICEPLUME coupled modeling system, which is hold on GitHub at https://github.com/ChuningWang/roms-iceplume. Configuration files and documents required to reproduce the results in this article are uploaded to a separate repository on GitHub (https://github.com/ChuningWang/roms-iceplume-test). Additionally, source code, configuration and model output files are openly available at https://doi.org/10.5281/zenodo.8192839.

References

Abib, N., Sutherland, D. A., Amundson, J. M., Duncan, D., Eidam, E. F., Jackson, R. H., et al. (2023). Persistent overcut regions dominate the terminus morphology of a rapidly melting tidewater glacier. *Annals of Glaciology*, 1–12. https://doi.org/10.1017/aog.2023.38

Baines, P. G. (2002). Two-dimensional plumes in stratified environments. *Journal of Fluid Mechanics*, 471, 315–337. https://doi.org/10.1017/s0022112002002215

Baines, P. G. (2008). Mixing in downslope flows in the ocean—Plumes versus gravity currents. Atmosphere-Ocean, 46(4), 405–419. https://doi.org/10.3137/ao.460402

Bao, W., & Moffat, C. (2023). Impact of shallow sills on heat transport and stratification regimes in proglacial fjords. *The Cryosphere Discussions*, 1–24.

Bartholomaus, T. C., Stearns, L. A., Sutherland, D. A., Shroyer, E. L., Nash, J. D., Walker, R. T., et al. (2016). Contrasts in the response of adjacent fjords and glaciers to ice-sheet surface melt in West Greenland. *Annals of Glaciology*, 57(73), 25–38. https://doi.org/10.1017/aog.2016.19
Beaird, N. L., Straneo, F., & Jenkins, W. (2018). Export of strongly diluted Greenland meltwater from a major glacial fjord. *Geophysical Research Letters*, 45(9), 4163–4170. https://doi.org/10.1029/2018gl077000

Carroll, D., Sutherland, D. A., Shroyer, E. L., Nash, J. D., Catania, G. A., & Stearns, L. A. (2017). Subglacial discharge-driven renewal of tidewater glacier fjords. *Journal of Geophysical Research: Oceans*, 122(8), 6611–6629. https://doi.org/10.1002/2017jc012962

Ching, C. Y., Fernando, H. J. S., & Noh, Y. (1993). Interaction of a negatively buoyant line plume with a density interface. *Dynamics of Atmospheres and Oceans*, 19(1–4), 367–388. https://doi.org/10.1016/0377-0265(93)90042-6

Cowton, T., Slater, D., Sole, A., Goldberg, D., & Nienow, P. (2015). Modeling the impact of glacial runoff on fjord circulation and submarine melt rate using a new subgrid-scale parameterization for glacial plumes. *Journal of Geophysical Research: Oceans*, 120(2), 796–812. https://doi.org/10.1002/2014jc010324

Ezhova, E., Cenedese, C., & Brandt, L. (2018). Dynamics of three-dimensional turbulent wall plumes and implications for estimates of submarine glacier melting. *Journal of Physical Oceanography*, 48(9), 1941–1950. https://doi.org/10.1175/jpo-d-17-0194.1

Farmer, D. M. (1978). Observations of long nonlinear internal waves in a lake. *Journal of Physical Oceanography*, 8(1), 63–73. https://doi.org/10.1175/1520-0485(1978)008<0063:oolniw>2.0.co;2

Fried, M. J., Catania, G. A., Bartholomaus, T. C., Duncan, D., Davis, M., Stearns, L. A., et al. (2015). Distributed subglacial discharge drives significant submarine melt at a Greenland tidewater glacier. *Geophysical Research Letters*, 42(21), 9328–9336. https://doi.org/10.1002/2015gl065806

WANG ET AL. 19 of 21

- Hager, A. O., Sutherland, D. A., Amundson, J. M., Jackson, R. H., Kienholz, C., Motyka, R. J., & Nash, J. D. (2022). Subglacial discharge reflux and buoyancy forcing drive seasonality in a silled glacial fjord. *Journal of Geophysical Research: Oceans*, 127(5),e2021JC018355. https://doi.org/10.1029/2021jc018355
- Haidvogel, D. B., Arango, H. G., Budgell, W. P., Cornuelle, B. D., Curchitser, E., Di Lorenzo, E., et al. (2008). Ocean forecasting in terrain-following coordinates: Formulation and skill assessment of the regional ocean modeling system. *Journal of Computational Physics*, 227(7), 3595–3624. https://doi.org/10.1016/j.jcp.2007.06.016
- Holland, D. M., & Jenkins, A. (1999). Modeling thermodynamic ice-ocean interactions at the base of an ice shelf. *Journal of Physical Oceanog-raphy*, 29(8), 1787–1800. https://doi.org/10.1175/1520-0485(1999)029<1787:mtioia>2.0.co;2
- Jackson, R. H., Motyka, R. J., Amundson, J. M., Abib, N., Sutherland, D. A., Nash, J. D., & Kienholz, C. (2022). The relationship between submarine melt and subglacial discharge from observations at a tidewater glacier. *Journal of Geophysical Research: Oceans*, 127(10), e2021JC018204. https://doi.org/10.1029/2021JC018204
- Jackson, R. H., Nash, J. D., Kienholz, C., Sutherland, D. A., Amundson, J. M., Motyka, R. J., et al. (2020). Meltwater intrusions reveal mechanisms for rapid submarine melt at a tidewater glacier. Geophysical Research Letters, 47(2), e2019GL085335. https://doi.org/10.1029/2019g1085335
- Jackson, R. H., Shroyer, E. L., Nash, J. D., Sutherland, D. A., Carroll, D., Fried, M. J., et al. (2017). Near-glacier surveying of a subglacial discharge plume: Implications for plume parameterizations. Geophysical Research Letters, 44(13), 6886–6894. https://doi.org/10.1002/2017gl073602
- Jenkins, A. (2011). Convection-driven melting near the grounding lines of ice shelves and tidewater glaciers. *Journal of Physical Oceanography*, 41(12), 2279–2294. https://doi.org/10.1175/jpo-d-11-03.1
- Kienholz, C., Amundson, J. M., Motyka, R. J., Jackson, R. H., Mickett, J. B., Sutherland, D. A., et al. (2019). Tracking icebergs with time-lapse photography and sparse optical flow, LeConte Bay, Alaska, 2016–2017. *Journal of Glaciology*, 65(250), 195–211. https://doi.org/10.1017/jog.2018.105
- Kilcher, L. F., & Nash, J. D. (2010). Structure and dynamics of the Columbia River tidal plume front. Journal of Geophysical Research, 115(C5), C05S90. https://doi.org/10.1029/2009jc006066
- Kimura, S., Holland, P. R., Jenkins, A., & Piggott, M. (2014). The effect of meltwater plumes on the melting of a vertical glacier face. *Journal of Physical Oceanography*, 44(12), 3099–3117. https://doi.org/10.1175/jpo-d-13-0219.1
- Mankoff, K. D., Straneo, F., Cenedese, C., Das, S. B., Richards, C. G., & Singh, H. (2016). Structure and dynamics of a subglacial discharge plume in a Greenlandic fjord. *Journal of Geophysical Research-Oceans*, 121(12), 8670–8688. https://doi.org/10.1002/2016jc011764
- McConnochie, C. D., Cenedese, C., & McElwaine, J. N. (2020). Surface expression of a wall fountain: Application to subglacial discharge plumes. *Journal of Physical Oceanography*, 50(5), 1245–1263. https://doi.org/10.1175/jpo-d-19-0213.1
- Mortensen, J., Lennert, K., Bendtsen, J., & Rysgaard, S. (2011). Heat sources for glacial melt in a sub-Arctic fjord (Godthabsfjord) in contact with
- the Greenland Ice Sheet. *Journal of Geophysical Research*, 116(C1), C01013. https://doi.org/10.1029/2010jc006528

 Morton, B. R., Taylor, G., & Turner, J. S. (1956). Turbulent gravitational convection from maintained and instantaneous sources. *Proceedings of*
- the royal society of London. Series A (Vol. 234, pp. 125–128).

 Motyka, R. J., Dryer, W. P., Amundson, J., Truffer, M., & Fahnestock, M. (2013). Rapid submarine melting driven by subglacial discharge,
- LeConte Glacier, Alaska. *Geophysical Research Letters*, 40(19), 5153–5158. https://doi.org/10.1002/grl.51011

 Mouginot, J., Rignot, E., Bjork, A. A., van den Broeke, M., Millan, R., Morlighem, M., et al. (2019). Forty-six years of Greenland Ice Sheet mass
- balance from 1972 to 2018. Proceedings of the National Academy of Sciences of the United States of America, 116(19), 9239–9244. https://doi.org/10.1073/pnas.1904242116
- Noh, Y., Fernando, H. J. S., & Ching, C. Y. (1992). Flows induced by the impingement of a 2-dimensional thermal on a density interface. *Journal of Physical Oceanography*, 22(10), 1207–1220. https://doi.org/10.1175/1520-0485(1992)022<1207:fibtio>2.0.co;2
- Oliver, H., Castelao, R. M., Wang, C., & Yager, P. L. (2020). Meltwater-enhanced nutrient export from Greenland's glacial fjords: A sensitivity analysis. *Journal of Geophysical Research: Oceans*, 125(7), e2020JC016185. https://doi.org/10.1029/2020jc016185
- Rignot, E., Fenty, I., Xu, Y., Cai, C., & Kemp, C. (2015). Undercutting of marine-terminating glaciers in West Greenland. Geophysical Research Letters, 42(14), 5909–5917. https://doi.org/10.1002/2015gl064236
- Sciascia, R., Straneo, F., Cenedese, C., & Heimbach, P. (2013). Seasonal variability of submarine melt rate and circulation in an East Greenland fjord. *Journal of Geophysical Research-Oceans*, 118(5), 2492–2506. https://doi.org/10.1002/jgrc.20142
- Slater, D. A., Nienow, P. W., Goldberg, D. N., Cowton, T. R., & Sole, A. J. (2017). A model for tidewater glacier undercutting by submarine melting. Geophysical Research Letters, 44(5), 2360–2368. https://doi.org/10.1002/2016gl072374
- Slater, D. A., Straneo, F., Das, S. B., Richards, C. G., Wagner, T. J. W., & Nienow, P. W. (2018). Localized plumes drive front-wide Ocean melting of a Greenlandic tidewater glacier. *Geophysical Research Letters*, 45(22), 12350–12358. https://doi.org/10.1029/2018gl080763
- Smolarkiewicz, P. K., & Margolin, L. G. (1998). MPDATA: A finite-difference solver for geophysical flows. *Journal of Computational Physics*, 140(2), 459–480. https://doi.org/10.1006/jcph.1998.5901
- Stevens, L. A., Straneo, F., Das, S. B., Plueddemann, A. J., Kukulya, A. L., & Morlighem, M. (2016). Linking glacially modified waters to catchment-scale subglacial discharge using autonomous underwater vehicle observations. *The Cryosphere*, 10(1), 417–432. https://doi.org/10.5194/tc-10-417-2016
- Straneo, F., & Cenedese, C. (2015). The dynamics of Greenland's Glacial Fjords and their role in climate. *Annual Review of Marine Science*, 7(1), 89–112. https://doi.org/10.1146/annurev-marine-010213-135133
- Straneo, F., & Heimbach, P. (2013). North Atlantic warming and the retreat of Greenland's outlet glaciers. *Nature*, 504(7478), 36–43. https://doi.org/10.1038/nature12854
- Sutherland, D. A., Jackson, R. H., Kienholz, C., Amundson, J. M., Dryer, W. P., Duncan, D., et al. (2019). Direct observations of submarine melt and subsurface geometry at a tidewater glacier. *Science*, 365(6451), 369, https://doi.org/10.1126/science.aax3528
- Thorpe, S. A. (1971). Asymmetry of the internal Seiche in Loch Ness. Nature, 231(5301), 306-308. https://doi.org/10.1038/231306a0
- Ungarish, M. (2010). An introduction to gravity currents and intrusions introduction. Introduction to Gravity Currents and Intrusions, 1-10.
- Warner, J. C., Sherwood, C. R., Arango, H. G., & Signell, R. P. (2005). Performance of four turbulence closure models implemented using a generic length scale method. *Ocean Modelling*, 8(1–2), 81–113. https://doi.org/10.1016/j.ocemod.2003.12.003
- Xu, Y., Rignot, E., Fenty, I., Menemenlis, D., & Flexas, M. M. (2013). Subaqueous melting of Store Glacier, west Greenland from three-dimensional, high-resolution numerical modeling and ocean observations. *Geophysical Research Letters*, 40(17), 4648–4653. https://doi.org/10.1002/grl.50825
- Xu, Y., Rignot, E., Menemenlis, D., & Koppes, M. (2012). Numerical experiments on subaqueous melting of Greenland tidewater glaciers in response to ocean warming and enhanced subglacial discharge. Annals of Glaciology, 53(60), 229–234. https://doi.org/10.3189/2012aog60a139

WANG ET AL. 20 of 21



Journal of Geophysical Research: Oceans

10.1029/2023JC019924

Zhao, K. X., Stewart, A. L., & McWilliams, J. C. (2022). Linking overturning, recirculation, and melt in glacial Fjords. *Geophysical Research Letters*, 49(15), e2021GL095706. https://doi.org/10.1029/2021gl095706

Zhao, K. X., Stewart, A. L., Mcwilliams, J. C., Fenty, I. G., & Rignot, E. J. (2023). Standing eddies in glacial fjords and their role in fjord circulation and melt. *Journal of Physical Oceanography*, 53(3), 821–840. https://doi.org/10.1175/jpo-d-22-0085.1

WANG ET AL. 21 of 21